Distinct transcriptomic profile of satellite cells contributes to preservation of neuromuscular junctions in extraocular muscles of ALS mice

Ang Li[1*], Jianxun Yi[1], Xuejun Li[1], Li Dong[1], Lyle W. Ostrow[2], Jianjie Ma[3], Jingsong Zhou[1*]

[1] Department of Kinesiology, College of Nursing and Health Innovation, University of Texas at Arlington, TX, 76019, USA

[2] Department of Neurology, Lewis Katz School of Medicine at Temple University, Philadelphia, PA 19122, USA

[3] Department of Surgery, Division of Surgical Sciences, University of Virginia, Charlottesville, VA, 22903, USA

* Corresponding author

Abstract

Amyotrophic lateral sclerosis (ALS) is a fatal neuromuscular disorder characterized by progressive weakness of almost all skeletal muscles, whereas extraocular muscles (EOMs) are comparatively spared. While hindlimb and diaphragm muscles of end-stage SOD1G93A (G93A) mice (a familial ALS mouse model) exhibit severe denervation and depletion of *Pax7*$^{+}$ satellite cells (SCs), we found that the pool of SCs and the integrity of neuromuscular junctions (NMJs) are maintained in EOMs. In cell sorting profiles, SCs derived from hindlimb and diaphragm muscles of G93A mice exhibit denervation-related activation, whereas SCs from EOMs of G93A mice display spontaneous (non-denervation-related) activation, similar to SCs from wild-type mice. Specifically, cultured EOM SCs contain more abundant transcripts of axon guidance molecules, including *Cxcl12*, along with more sustainable renewability than the diaphragm and hindlimb counterparts under differentiation pressure. In neuromuscular co-culture assays, AAV-delivery of *Cxcl12* to G93A-hindlimb SC-derived myotubes enhances motor neuron axon extension and innervation, recapitulating the innervation capacity of EOM SC-derived myotubes. G93A mice fed with sodium butyrate (NaBu) supplementation exhibited less NMJ loss in hindlimb and diaphragm muscles. Additionally, SCs derived from G93A hindlimb and diaphragm muscles displayed elevated expression of *Cxcl12* and improved renewability following NaBu treatment *in vitro*. Thus, the NaBu-induced transcriptomic changes resembling the patterns of EOM SCs may underlie the beneficial effects observed in G93A mice. More broadly, the distinct transcriptomic profile of EOM SCs may offer novel therapeutic targets to slow progressive neuromuscular functional decay in ALS and provide possible "response biomarkers" in pre-clinical and clinical studies.

Key words: amyotrophic lateral sclerosis, satellite cell, neuromuscular junction, chemokine.

Abbreviations: acetylcholine receptor (AChR); amyotrophic lateral sclerosis (ALS); extensor digitorum longus (EDL); extraocular muscle (EOM); flexor digitorum brevis (FDB); hindlimb (HL); motor neuron (MN); neuromuscular junction (NMJ); tibialis anterior (TA); sodium butyrate (NaBu).

Introduction

Amyotrophic lateral sclerosis (ALS) is a fatal disorder characterized by progressive motor neuron (MN) loss and skeletal muscle wasting, resulting in respiratory failure and death 3–5 years following diagnosis [1,2]. While not entirely spared, the extraocular muscles (EOMs) of ALS patients and mutant mouse models exhibit comparatively preserved structure and function and retained neuromuscular junctions (NMJ) [3-6]. The reason for this differential involvement remains unclear, especially considering that eye movements are preferentially involved in other neuromuscular disorders like myasthenia gravis, some muscular dystrophies, and mitochondrial myopathies [7,8].

While ALS is classically considered predominantly a “dying-forward” process of motor neurons (MN), accumulated evidence [9-17] support that early muscle dysfunction is an important contributor to ALS pathophysiology. The degree to which “dying-forward” from the central nerve system or “dying-back” process [18-20] starting distally at NMJs contributing to ALS progression remains unsettled and may vary in different patient subsets. Regardless of the direction of communication and relative contribution of different cell types to ALS progression (e.g. glia, neurons, myofibers) [20], it is widely accepted that NMJ disassembly and the resulting skeletal muscle denervation is a critical pathogenic event in both patients and animal models [21-24].

EOMs differ from limb and trunk muscles in many respects [25]. In contrast to other skeletal muscles, the individual motor neurons (MNs) controlling EOMs innervate fewer EOM myofibers, and individual myofibers often have multiple NMJs [26]. The multiple innervation phenotype refers to the co-existence of innervated "en plaque" and "en grappe" NMJs in a single EOM myofiber. The "en plaque" type of NMJs are located in the middle portion of myofibers and resemble NMJs seen in other types of muscles. Each EOM myofiber has one "un plaque" NMJ. "en grappe" NMJs are a series of smaller, grape-shaped NMJs that are located in the distal portion of some EOM myofibers [3,26]. MNs innervating EOMs express higher level of the Ca^{2+} binding proteins calbindin-D28k and parvalbumin, thus may be more resistant to the Ca^{2+}-induced excitotoxicity [27-29]. The expression profile of EOM myofibers is also different from that of limb muscle in over 300 genes [30]. Previous studies have investigated the muscle-derived neuroprotective factors, including BDNF, GDNF, NT3 and NT4 and found that none of these classical neurotrophic factors was expressed (RNA or proteins) significantly higher in EOM myofibers compared to hindlimb myofibers in both mutant G93A and wild-type mice [31,32]. Thus, it is important to look for clues in other cell types that influence the microenvironment around NMJs, such as satellite cells (SCs).

An association between SC function, NMJ integrity, and resultant denervation has been demonstrated in animal models of aging and muscular dystrophy [33,34]. Using transgenic mice expressing GFP in the progeny of activated SCs, Liu and colleagues demonstrated that inducible depletion of adult skeletal muscle SCs impaired the regeneration of NMJs [33]. Furthermore, they found that the loss of SCs exacerbated age-related NMJ degeneration. Preservation of SCs attenuated aging-related NMJ loss and improved muscle performance in mice [34]. SCs from EOMs exhibit superior expansion and renewability (the capability to maintain dividing and undifferentiated stem cells after rounds of regeneration) than their limb counterparts [35], inspiring us to compare the phenotypes of SCs derived from EOMs and limb muscles and to conduct transcriptomic profiling of SCs to look for candidate genes that could preserve NMJ integrity in ALS.

In the current study, we found that the integrity of NMJs and the amount of $Pax7^{+}$ SCs are maintained in EOMs in end-stage G93A mice, in contrast to the severe denervation and depletion of

Pax7$^+$ SCs in hindlimb and diaphragm muscles. Transcriptomic profiling revealed that the EOM SCs exhibit abundant transcripts of axon guidance molecules, such as *Cxcl12*, along with sustainable renewability compared with SCs from diaphragm and hindlimb muscles. Furthermore, EOM SC-derived myotubes enhance axon extension and innervation in co-culture experiments with spinal motor neurons compared to hindlimb SC-derived myotubes. Overexpressing *Cxcl12* using adeno-associated viral vector (AAV8) in G93A hindlimb SC-derived myotubes recapitulated features of the EOM SC-derived myotubes.

Butyrate, a short-chain fatty acid produced by bacterial fermentation of dietary fibers in the colon, has been shown to extend the survival of ALS G93A mice [36]. We found that G93A mice fed with 2% sodium butyrate (NaBu) in drinking water decreased NMJ denervation and SC depletion in hindlimb and diaphragm muscles. Adding NaBu to the culture medium improved the renewability of SCs derived from the G93A hindlimb and diaphragm muscles, as well as increasing the expression of *Cxcl12,* resembling EOM SC transcriptomic pattern. Since muscle tissue can be biopsied during life, characterizing the distinct EOM SC transcriptomic pattern could provide potential predictive/cohort selective, and response/pharmacodynamic biomarkers in therapeutic trials in both ALS patients and animal models, in addition to identifying therapeutic targets.

Results

NMJ integrity and peri-NMJ SC abundance are preserved in EOMs, and NaBu-supplemented feeding reduces NMJ denervation and SC depletion in hindlimb and diaphragm muscles in G93A mice

We investigated the NMJ integrity and peri-NMJ SC abundance by whole-mount imaging of extensor digitorum longus (EDL), soleus, diaphragm, and EOMs derived from WT littermates and G93A mice with or without NaBu-supplemented feeding. For EOMs, only the “en plaque” type of NMJs were included in this comparison, because they resemble NMJs in other types of muscles in morphology and spatial distribution. The “en grappe” type of NMJs were not included. Z-stack scans of glycerol-cleared whole muscles were obtained using a high working distance lens in a confocal microscope. The z-stacks were compacted into 2D images by maximal intensity projection. Acetylcholine receptors (AChRs) at NMJs were labeled with Alexa Fluor conjugated α-Bungarotoxin (BTX). Axons and axon terminals of motor neurons were labeled with antibodies to neurofilament (NF) and synaptophysin (SYP) respectively (**Figure 1A** and **Figure 1-figure supplement 1A**). In order to quantify the extent of denervation in a categorical manner, NMJs were arbitrarily defined as “well innervated” if SYP staining was present in >60% of the BTX positive area, “partially innervated” if between 60% and 30%, and “poorly innervated” if SYP staining corresponded to less than 30% of the BTX positive area. Poorly innervated NMJs also generally lacked nearby NF$^+$ axons (**Figure 1-figure supplement 1A**).

At least 343 (average 758 ± 345 per group) NMJs from muscles (EDL, soleus, diaphragm and EOMs, respectively) dissected from WT or G93A mice with or without NaBu-feeding were examined (**Figure 1-table supplement 1**) in order to calculate the relative proportions of well-, partially- and poorly-innervated NMJs (**Figure 1B**). EDL, soleus and diaphragm muscles, but not EOMs, from end stage G93A mice (4-month-old) exhibited significant decrease in well-innervated NMJs, accompanied by an increase in poorly-innervate NMJs. The increase of “poorly-innervated NMJ” is slightly less dramatic in diaphragm compared to the hindlimb muscles, meanwhile the increase of “partially-innervated NMJ” ratio is the most significant in the diaphragm (**Figure 1B**), indicating that denervation process is most severe in hindlimb muscles, slightly milder in diaphragm and barely detectable in EOMs. Consistent

with previous observation by our lab and others that NaBu treatment slows ALS progression [36], the hindlimb and diaphragm muscles from NaBu-fed mice (1 month, 2% in water, starting feeding at the age of 3-month-old) all exhibited significantly reduced denervation compared to littermates who were not fed NaBu (**Figure 1B**, n = 10 per group, gender matched).

qRT-PCR for *Scn5a*, the gene encoding sodium channel Nav1.5, was performed with RNA extracted from whole muscles and used as another marker of denervation [37-39] **(Figure 1-figure supplement 1B**). The original values of *Scn5a* expression levels are provided in **Figure 1-table supplement 2**. Consistent with the immunostaining quantification in **Figure 1A**, the elevation of *Scn5a* expression is most notable when comparing G93A hindlimb muscles to wildtype counterparts (>250 folds for EDL, >70 folds for soleus), milder for diaphragm (> 15 folds) and not significant for EOMs. Additionally, NaBu feeding significantly reduced the *Scn5a* transcripts in hindlimb muscles (**Figure 1-figure supplement 1B**).

Whole mount imaging of muscles stained with the satellite cell (SC) markers Pax7, BTX, SYP, and DAPI, was used to quantify SCs in the vicinity of NMJs. The Pax7 signal in each z-stack image was filtered using DAPI as a mask to identify $Pax7^+$ cell nuclei. Afterwards the z-stacks were compacted into 2D images by maximal intensity projection (**Figure 2A**). The number of nuclear $Pax7^+$ cells were counted within the circles of 75 µm diameter drawn around the NMJs (**Figure 2B**, see also **Figure 2-table supplement 1)**. Similar to the NMJ denervation status, depletion of peri-NMJ SCs was most significant in hindlimb muscles of end-stage G93A mice and slightly milder in diaphragm, while no significant depletion was observed in EOMs (**Figure 2C**). G93A mice fed with NaBu had less depletion of SCs in hindlimb and diaphragm muscles.

The proliferation and differentiation properties are conserved in SCs derived from G93A EOMs

We conducted FACS based isolation of SCs from hindlimb (combining tibialis anterior, EDL, quadriceps and gastrocnemius), diaphragm, and EOMs using a modified version of a published protocol [40]. Soleus was excluded because it has higher content of slow-twitch myofibers (37-55%), which is more similar to diaphragm than the other fast-twitch fiber-dominant hindlimb muscles [41-44]. Vcam1 was used as a marker for quiescent SC. CD31 (endothelial cell marker), CD45 (hematopoietic cell marker) and Sca-1 (mesenchymal stem cell marker) positive cells were discarded. Thus, in the FACS profile the target SC population ($Vcam1^+CD31^-CD45^-Sca\text{-}1^-$) was in gate P5-4 (**Figure 3A**). Single antibody staining controls are shown in **Figure 3-figure supplement 1**. We also applied methyl-green (20 µg/ml) staining [45] to evaluate the viability of cells (**Figure 3-figure supplement 2**), only about 1% of Vcam1 positive population were methyl green stained (**Figure 3-figure supplement 2D**, Events P5-2 / (P5-2 + P5-4)*100%). Thus, most cells were alive when loaded into the flow cytometer.

SCs isolated from WT hindlimb and diaphragm muscles exhibited relatively homogenous levels of Vcam1, which facilitated separation from other cells and debris (**Figure 3A**, gate P5-4), and also indicates they are mostly quiescent under resting conditions. In contrast, SCs derived from the G93A hindlimb and diaphragm displayed heterogeneous levels of Vcam1, potentially due to ongoing activation/differentiation triggered by disease progression (**Figure 3A**). Importantly, EOM SCs from both WT and G93A mice were heterogeneous in Vcam1 levels, implying they are spontaneously activated even in the absence of pathological stimulation (**Figure 3A**). While significant decreases of P5-4 population were observed in the G93A hindlimb and diaphragm derived SCs compared to WT, no significant difference was detected between G93A and WT EOM derived SCs (**Figure 3B**).

FACS-isolated SCs were next cultured in growth medium for 4 days, fixed, and stained for MyoD to confirm their myogenic lineage. Close to 100% of the cells were MyoD positive (**Figure 4A**). We examined the ratio of actively proliferating cells ($Ki67^+$) among the SCs (labeled with Pax7) [46]. SCs

isolated from both WT and G93A EOMs exhibited the highest Pax/Ki67 double positive ratio, and the lowest Pax7/Ki67 double negative ratio (**Figure 4A**). These observations are consistent with previous reports of superior proliferative potential of EOM SCs compared to limb and diaphragm muscles [35]. The direct comparison between WT and G93A muscle SCs is presented in **Figure 4-figure supplement 1**.

We also compared myotube formation and cell proliferation of cultured SCs under differentiation conditions. After 4 days in growth medium, we switched to differentiation medium and cultured the cells for 2 more days. The cells were then stained for sarcomere myosin heavy chain (MHC), Pax7 and Ki67. The EOM-derived SCs exhibited a higher number of Pax7 positive cells ($Pax7^+/Ki67^+$ and $Pax7^+/Ki67^-$) compared to SCs derived from hindlimb and diaphragm muscles – from both WT and G93A mice (**Figure 4B**). In contrast, the fusion indices, which calculate the ratio of nucleus within the MHC positive myotubes, were the lowest for EOM SCs (**Figure 4B**). This does not necessarily mean the EOM SCs have deficiencies in differentiation after they are committed, but more likely a reflection of their superior preservation of actively proliferating population [47]. In support of this view, previous TA engraftment experiments showed that more myofibers were generated by EOM SCs than their limb counterparts [35].

Butyrate induces EOM-like preservation of renewability in FACS-isolated SCs under differentiation conditions *in vitro*

Since NaBu-supplemented feeding reduced SC depletion in end stage G93A mice (**Figure 2**) *in vivo*, we tested NaBu treatment on cultured SCs. G93A hindlimb SCs were cultured with 0, 0.1, 0.5, 1.0, 2.5 and 5 mM of NaBu added to the growth medium for 1 day. RNAs were collected for qRT-PCR to evaluate the short-term impact of NaBu on cell growth. The relative expression of the proliferation markers (*HMGA2* and *CCND1*) peaked at 0.5 mM. In contrast, the relative expression of proliferation inhibitor P21 bottomed at 0.5 mM (**Figure 5A**), indicating 0.5 mM as the optimal concentration of NaBu application *in vitro*.

We designed two NaBu treatment plans for G93A diaphragm and hindlimb SCs as follows: one with 0.5 mM NaBu applied in the growth medium for 1 day before switching to differentiation medium (1 day in growth medium), the other with NaBu continuously applied for 3 days (1 day in growth medium + 2 days in differentiation medium). As shown in **Figure 5B**, the G93A hindlimb and diaphragm SCs in culture showed significant increase in the ratio of Pax7 positive cells under the 1-day NaBu treatment, associated with a decrease in fusion index. This trend was more pronounced under the 3-day NaBu treatment. These data indicate that NaBu treatment results in EOM-like preservation of renewability of the G93A SCs (**Figure 4B**). Aside from the drop of fusion indices after 3-day treatment with NaBu, there was notable decrease of MHC levels, indicating long-term exposure to NaBu did inhibit the differentiation process (**Figure 5B**), which is in line with the published result observed in C2C12 cells [48].

EOM-derived SCs show distinct transcriptome profile supporting self-renewal and axonal growth when compared to the SCs derived from other muscle origins

We extracted RNAs from SCs of hindlimb, diaphragm and EOMs under the following two culture conditions: first, in growth medium for 4 days (with suffix “G”); second, in growth medium for 4 days and then in differentiation medium for 2 days (with suffix “D”). The RNAs were send for bulk RNA-Seq. Additionally, RNA-Seq analyses were conducted for SCs of G93A hindlimb and diaphragm muscles cultured with NaBu for 3 days (with suffix “NaBu3”) (**Figure 6**).

Similarities of the transcriptomic profiles of RNA-Seq samples were examined using the Principle Component Analysis (PCA) and hierarchical clustering (**Figure 6A**). We found that both WT and G93A EOM SCs cultured in differentiation medium were more similar to hindlimb and diaphragm SCs in growth medium than their counterparts in differentiation medium, highlighting the superior renewability of EOM SCs in differentiation medium and is consistent with the immunostaining results showed in **Figure 4B**.

To understand RNA-Seq data in the perspective of SC homeostasis, which refers to the transition between quiescence (dormant, slow self-renewal), activation (rapid amplification with symmetric and asymmetric cell division) and differentiation states during tissue regeneration [47], we compiled the lists of quiescence, activation and differentiation signature genes respectively. For quiescence signature genes, a list of 507 genes highly upregulated in quiescent SCs compared to activated SCs have been generated previously by Fukada et al [49]. We adopted this list together with other 18 genes denoted by other investigators, including *Notch1*, *Notch2*, *Hes1*, *Hey1*, *Rbpj*, *Dtx4*, *Jag1*, *Sox8*, *Sdc3*, *Itga7*, *Itgb1*, *Met*, *Vcam1*, *Ncam1*, *Cdh2*, *Cdh15*, *Cxcr4*, *Cav1* [47,50-53]. The activation signature gene list was generated from our RNA-seq data using those expressed significantly higher in SCs (both from WT and G93A) in growth medium (1187 genes in total, $|\log2FC| \geqslant 0.4$ and FDR $\leqslant 0.001$). Accordingly, the differentiation signature gene list was generated from those expressed significantly higher in SCs cultured in differentiation medium (1349 genes in total).

To verify that our signature gene lists recapitulate the SC properties at activation and differentiation state reported in previous studies, we did functional annotation analysis (KEGG pathway, Gene ontology_biological process, Gene ontology_cellular component). As shown in **Figure 6-figure supplement 1,** the top functional annotations enriched in our activation signature genes are all related to cell cycle and DNA replication, while the top functional annotations for our differentiation signature genes are associated with muscle contraction, muscle-specific subcellular structures and metabolic changes.

To explore whether the homeostatic states of EOM SCs are different from that of SCs from other muscle origins, we looked for differentially expressed genes (DEGs) shared-in-common among the following four groups: WT EOM SC-vs-WT diaphragm SC; WT EOM SC-vs-WT HL SC; G93A EOM SC-vs-G93A diaphragm SC; G93A EOM SC-vs-G93A HL SC (**Figure 6B**, left two panels). Within the 1119 shared DEGs identified in SCs cultured in growth medium, slightly more activation signature genes and quiescence signature genes were expressed higher in EOM SCs compared to diaphragm and HL derived SCs. Meanwhile more differentiation signature genes were expressed lower in EOM SCs (**Figure 6C**, leftmost panel and **Figure 6-table supplement 1**). These trends became much more prominent in the 3318 shared DEGs identified in SCs cultured in differentiation medium, implying that EOM SCs are notably superior at preserving renewability in a differentiation environment than their diaphragm and hindlimb counterparts (**Figure 6C**, middle panel). Consistently, subgroups of quiescence signature genes belonging to commonly used stem cell markers (*Pax7, Cd34, Cxcr4, Vcam1, Sdc3, Sdc4, Cdh15, Met, Cav1*), Notch signaling pathway (*Notch1, Notch2, Notch3, Jag1, Heyl, Dtx4, Msc*) and pluripotency signaling pathway (*Klf4, Igf1, Bmp2, Bmp4, Fzd4, Fgfr4, Pik3r1, Lifr*) were all expressed higher in EOM SCs in differentiation medium than SCs derived from diaphragm and hindlimb muscles (**Figure 6C**, middle panel and **Figure 6-table supplement 2**).

In parallel, we examined whether the 3-day NaBu treatment could alter the homeostasis of G93A diaphragm and hindlimb SCs (**Figure 6B**, rightmost panel). There were 3018 DEGs shared between the following two comparing groups: G93A diaphragm SC_D_NaBu3-vs-G93A diaphragm SC_D and G93A HL SC_D_NaBu3-vs-G93A HL SC_D. Similar to the trends observed in EOM SCs in differentiation medium, the majority of activation and quiescence signature genes found in these DEGs were upregulated in the NaBu treated group, while the differentiation signature genes were

downregulated (**Figure 6C**, rightmost panel). The elevated quiescence signature genes of the NaBu treated group include commonly used stem cell markers (*Pax7, Cd34, Vcam1, Sdc4, Cdh2, Met, Cav1, Itga7*), Notch signaling pathway members (*Notch3*, *Rbpj*) and pluripotency signaling pathway components (*Fzd4*, *Bmp4*). However, other three pluripotency related genes (*Klf4*, *Wnt4* and *Bmp2*) were found downregulated (**Figure 6-table supplement 3**), indicating that NaBu treatment also has a mixed impact on the stemness of the SCs.

To compile EOM SCs signature gene list, we identified 621 genes expressed higher in EOM SCs than diaphragm and hindlimb SCs cultured in growth medium from the 1119 DEGs (**Figure 6B,** leftmost panel). Next, we pulled out 2424 genes that are expressed higher in EOM SCs than diaphragm and hindlimb SCs cultured in differentiation medium from the 3318 DEGs (**Figure 6B,** middle panel). These two lists have 478 genes shared-in-common. Particularly, many of these genes are related to axon guidance, cell migration and neuron projection (**Figure 7A**)**. Figure 7A-figure supplement 1**, **Figure 7-table supplement 1 and 2** further demonstrate this phenotype when the functional annotation analysis was done separately for the growth or differentiation culture conditions. The functional annotation analysis for the 3018 genes altered by the 3-day NaBu treatment (**Figure 6B**, rightmost panel) also spotted axon guidance, cell migration and neuron projection on the top of the annotation lists (**Figure 7B** and **Figure7-table supplement 3**). Importantly, the chemokine *Cxcl12* shows up in all three lists. Cxcl12 is known to promote axonal extension and NMJ regeneration [54]. These data suggest that enhanced attraction of motor neuron axons by peri-NMJ SCs might be a shared mechanism underlying the NMJ preservation in EOMs and NaBu treatment observed in G93A mice.

We selected one representative gene from each of the following categories: activation (*Hmga2*), differentiation (*Actn3*) and quiescence (*Notch3*) signature genes, as well as an axon guidance gene (*Cxcl12*) for qRT-PCR. For each muscle type and culture condition, we collected samples from 3-6 rounds of sorting (the individual results are listed in **Figure 7-table supplement 4-6**). We observed significantly higher expression of *Hmga2* in EOM SCs compared to diaphragm and hindlimb SCs cultured in either growth or differentiation medium (**Figure 7C**, leftmost panel), confirming the superior renewability of EOM SCs. The 3-day NaBu treatment of diaphragm and hindlimb SCs derived from G93A mice also upregulated *Hmga2* (**Figure 7D**, leftmost panel). *Actn3* was expressed lower in EOM SCs than diaphragm SCs cultured in either growth or differentiation medium, but not necessarily lower than hindlimb SCs (**Figure 7C**, 2nd panel from the left). Meanwhile NaBu treatment significantly decreased *Actn3* expression (**Figure 7D**, 2nd panel from the left). Consistent with the RNA-Seq data, the quiescence marker *Notch3* was expressed significantly higher in EOM SCs than diaphragm and hindlimb SCs cultured in differentiation medium but not in growth medium (**Figure 7C**, 2nd panel from the right). Similarly, NaBu treatment also elevated *Notch3* expression (**Figure 7D**, 2nd panel from the right) in G93A diaphragm and hindlimb SCs cultured in differential medium. Importantly, the axon guidance molecule *Cxcl12* was expressed significantly higher in EOM SCs than diaphragm and hindlimb SCs cultured in both growth and differentiation medium (**Figure 7C**, rightmost panel). NaBu treatment elevated *Cxcl12* expression as well (**Figure 7D**, rightmost panel), confirming enhanced axon attraction as a common feature shared by EOM SCs and NaBu treatment.

AAV mediated overexpression of *Cxcl12* in myotubes promotes motor neuron axon extension

Since recombinant *Cxcl12* is known to promote axon extension [54], we tested whether overexpressing *Cxcl12* in myotubes via adeno-associated virus (AAV) transduction could achieve the same effect. For these experiments, we co-cultured motor neurons and SC-derived myotubes on compartmentalized microfluidic chambers (XonaChip). Because AAV vectors do not transduce satellite cells efficiently [55,56], we first seeded the satellite cells into one compartment of the XonaChips, then induced them to differentiate for two days before AAV transduction. Four types of AAV-transduced

myotubes were used for the coculture assays: a) WT hindlimb SC-derived myotubes transduced with AAV-CMV-eGFP; b) G93A hindlimb SC-derived myotubes transduced with AAV-CMV-eGFP; c) G93A hindlimb SC-derived myotubes transduced with AAV-CMV-Cxcl12-IRES-eGFP; and d) G93A EOM SC-derived myotubes transduced with AAV-CMV-eGFP. One day after AAV transduction, rat spinal motor neurons (RSMN) were seeded into the other compartment of the XonaChips and the culture medium switched to Neurobasal Plus Medium (NBPM) (**Figure 8A**). The cocultures were maintained for 9 more days. Immunostaining confirmed increased presence of Cxcl12 protein in the form of cytosolic vesicles in myotubes transduced with AAV8-CMV-Cxcl12-IRES-eGFP but not those transduced with AAV8-CMV-eGFP (**Figure 8-figure supplement 1**). These are likely vesicles for secretion [57].

By measuring the lengths of the longest RSMN neurites (presumably axons) crossing the 450 µm microgrooves, we noticed that hindlimb-SC derived myotubes from G93A mice, but not from WT littermates, appeared repulsive to distal axons. The axons stayed close to the edge of the microgrooves and even grew backward towards the neuronal compartment, which we termed “edge effect” (**Figure 8B** and **Figure 8-figure supplement 2A**, arrows). This was rarely seen in the WT hindlimb SC-derived myotubes. In contrast, RSMN axon extension was dramatically enhanced in the co-culture system either with G93A hindlimb SC-derived myotubes overexpressing *Cxcl12*, or G93A EOM SC-derived myotubes overexpressing GFP (as control) (**Figure 8B, C**). Those neurites located close to the microgrooves were often seen to closely grow along nearby myotubes (**Figure 8-figure supplement 2B**). G93A hindlimb SC-derived myotubes overexpressing *Cxcl12* occasionally were even seen to overcome the “edge effect” and redirect the axons towards their proximities (**Figure 8-figure supplement 2B**, arrow) - a persuasive indication of chemoattractive effects of those myotubes. Meanwhile, RSMN innervation of AChR clusters (BTX positive patches) were not seen in co-cultures with G93A hindlimb SC-derived myotubes overexpressing GFP, while they were consistently observed in the other three types of AAV-transduced myotubes (**Figure 8C**).

The overall innervation incidence was too low for statistical analysis due to the sparsity of axons in the myotube compartments, thus we conducted co-culture experiments where RSMNs were added to SC-derived myotubes in a uni-compartmental co-culture setting. As shown in **Figure 9A-C** and **Figure 9-figure supplement 1A-C**, when co-cultured in a single compartment, *Cxcl12* overexpressing G93A hindlimb SC-derived myotubes exhibited increased innervation compared to GFP overexpressing controls. Furthermore, individual *Cxcl12* overexpressing EOM SC derived myotubes were frequently innervated by multiple (3 or more) times (**Figure 9A-C** and **Figure 9-figure supplement 1D**), recapitulating the “multi-innervation” property of EOMs *in vivo* [26]. The extra “anchor points” seemed to encourage better spatial alignment of the RSMN axon network to the myotubes globally in the co-cultures. This spatial alignment of RSMN axons and myotubes was not observed in co-cultures of RSMNs and hindlimb SC-derived myotubes (*without Cxcl12 overexpression*), which also did not exhibit multi-innervation (**Figure 9A-C** and **Figure 9-figure supplement 1A-C**). Under higher magnification, we often observed that axons sending branches to adjacent BTX positive patches on EOM SC-derived myotubes (**Figure 9B**, arrows). Of note, there was higher expression of several Netrin and Semaphorin family members reported to promote axon-branching in EOM SCs compared to other muscle-derived SCs cultured in differentiation medium (**Figure 7-table supplement 2**) [58-63]. This milieu, comprised of abundant axon guidance molecules, in combination with the robust self-renewability of satellite cells, may contribute to the relative EOM NMJ resistance in ALS.

Discussion

We have demonstrated an association between the degeneration of NMJs and depletion of peri-NMJ SCs in hindlimb and diaphragm muscles *in vivo* in end-stage G93A mice. In contrast, EOM NMJs exhibited no signs of denervation or SCs depletion. The FACS profile of SCs isolated from EOM suggests spontaneous activation even without pathological stimulation, which is supported by previous *in vivo* BrdU labeling and staining results [64]. Furthermore, immunostaining, qRT-PCR and RNA-Seq analyses all imply that EOM SCs *in vitro* possess superior renewability better than hindlimb and diaphragm SCs, under differentiation-inducing culture conditions. Comparative functional annotation analyses of the transcriptomes highlight higher expression of axon guidance molecules in EOM SCs. Neuromuscular coculture experiments demonstrate that EOM SC-derived myotubes are more attractive to potential axons derived from rat spinal motor neurons than their hindlimb counterparts – which in fact appeared to repel the branching axons. Thus, the unique homeostasis regulation and axon attraction properties of EOM SCs may contribute to the resistance to denervation of EOM under ALS (**Figure 9D**).

Earlier report of SC quantification from muscle biopsy samples using electron microscopy detected no significant difference between ALS patients and non-ALS controls [65]. Other studies using primary cultured SCs from muscle biopsy samples implied compromised differentiation program in ALS SCs compared to controls [66,67]. As to proliferation, one study reported enhanced proliferation in ALS SCs [67], while the other cued for deficits in proliferation in ALS SCs [66]. The various findings may reflect variations in the disease stage of patients during sampling. For animal studies, Manzano *et al* measured the amount of Pax^{7+} SCs in dissociated EDL and soleus myofibers from G93A mice and WT controls and observed large variations across muscle-type and disease stage [68]. In another study carried out by the same group, primarily cultured EDL and soleus SCs from G93A mice generally showed lower proliferation potential than the WT counterparts [69].

In our whole-mount muscle imaging data and FACS profiles of isolated SCs, SC depletion, at least for the most quiescent population, is observed in hindlimb and diaphragm muscles from end-stage G93A mice. Additionally, the heterogeneity of Vcam1 levels observed in hindlimb and diaphragm SCs derived from end stage G93A mice compared to those from WT controls indicates occurrence of denervation-related pathological activation. Although this activation may transiently elevate the number of SCs, the continuous dominance of asymmetric over symmetric cell division, as well as the differentiation pressure to regenerate myofibers could gradually exhaust the quiescent stem cell pool, leading to the depletion phenotype seen in the end stage G93A mice. In contrast, the superior preservation of renewability of EOM SCs seen in differentiation medium is an effective measure against this catastrophe. However, the spontaneous activation and superior renewability of EOM SCs may not always be an advantage. As mentioned in the introduction section, EOMs are preferentially involved in some other neuromuscular disorders. In the case of mitochondrial myopathies, mitochondrial DNA defects accumulate over time, resulting in compromised oxidative phosphorylation represented by cytochrome c oxidase (COX) deficient myofibers in patients [7,8]. The proportion of COX-deficient myofibers is higher in EOMs than other muscles, which may be related to accelerated spreading of mitochondrial DNA defects in myofibers by the distinct properties of EOM SCs.

In this study, overexpressing *Cxcl12* in G93A hindlimb SC-derived myotubes promotes motor neuron axon extension under the co-cultured condition. *Cxcl12* has been known as a critical axon guidance cue for motor neurons during development [70,71]. In adult animals, peri-synaptic Schwann cells have recently been reported to transiently produce *Cxcl12* after acute motor axon terminal degeneration [54]. Intraperitoneal injection of antibodies neutralizing secreted Cxcl12 protein slows down the regeneration process. In contrast, the exposure of primary motor neurons to recombinant Cxcl12 protein stimulates neurite outgrowth and directional axonal extension in compartmentalized

culture setup, which could be reversed by the treatment of the Cxcr4 specific inhibitor AMD3100 [54]. Since myoblasts also express *Cxcr4* and will migrate along the Cxcl12 protein gradient during muscle regeneration [72,73], the abundant peri-NMJ SCs in EOM expressing *Cxcl12* may achieve synergistic effect with peri-synaptic Schwann cells, improving the long-term integrity of NMJs.

Epigenetic regulation of SC transcriptome by histone deacetylase (HDAC) inhibitors, such as butyrate [74], could modulate the myogenesis process both *in vitro* and *in vivo* [48,75-77]. Butyrate is a gut-bacteria fermentation product that also acts as an energy source to improve mitochondrial respiration [74,78]. Previous studies by our lab and others showed NaBu-supplemented feeding prolongs the life span of G93A mice and reverses CypD-related mitoflash phenotypes in myofibers derived from G93A mice, which implies a potential decrease of oxidative stress. Additionally, NaBu treatment also improved mitochondrial respiratory function of NSC34 motor neuron cell line overexpressing hSOD1G93A [36,79,80]. Yet it was not known whether the beneficiary effects of NaBu are linked to any phenotypic changes of SCs, and whether NaBu treatment induced epigenetic modulations similar to that of EOM SCs. The study here revealed its beneficiary role on the preservation of NMJ integrity and peri-NMJ SCs affected in hindlimb and diaphragm muscles by ALS progression. NaBu treatment of G93A hindlimb and diaphragm SCs in culture induced transcriptomic changes mimicking some features seen in EOM SCs, including the upregulation of activation and quiescence signature genes and the downregulation of differentiation signature genes, indicating NaBu improved the renewability of G93A hindlimb and diaphragm SCs. Additionally, some axon guidance molecules, particularly *Cxcl12*, were also induced by NaBu application (**Figure 9D**). Thus, NaBu-induced EOM SC-like transcriptomic pattern could be a crucial contributor to its therapeutic effect against ALS progression.

Overall, our studies have defined several mechanisms which (1) may explain why EOMs are relatively spared in ALS, and (2) provides a rationale for targeting these differences as a therapeutic strategy. Furthermore, analysis of these signatures in patient muscle biopsies could be used to select subsets of ALS patients who may be most likely to benefit from therapies targeting this signaling network, and to provide possible "response biomarkers" in pre-clinical and clinical studies. As a cocktail of sodium phenylbutyrate (a derivative of NaBu) and Taurursodiol (an antioxidant) under the Commercial name of Relyvrio has been recently approved in US and Canada as a new ALS therapy [81], our study could help gain more insights into the molecular mechanisms related to this type of ALS therapy.

Materials and methods

Animals

All animal experiments were carried out in accordance with the recommendations in the *Guide for the Care and Use of Laboratory Animals* of the National Institutes of Health. The protocol on the usage of mice was approved by the Institutional Animal Care and Use Committee of the University of Texas at Arlington (A19.001, approval date: 09/20/2018). WT mice used in this study were of B6SJL background. The ALS transgenic mouse model (hSOD1G93A) with genetic background of B6SJL was originally generated by Drs. Deng and Siddique's group at Northwestern University and deposited to the Jackson Lab as B6SJL-Tg (SOD1*G93A) [82]. For the butyrate feeding experiment, the animals were fed with 2% NaBu from the age of 3 months (at the ALS disease onset) and lasting for 4 weeks.

Primary culture of satellite cells isolated by fluorescence-activated cell sorting

The hindlimb muscles including tibialis anterior (TA), extensor digitorum longus (EDL), gastrocnemius, and quadriceps were dissected from 1-2 mice. For diaphragm, both the crural and costal domains were dissected from 1-2 mice. For EOMs, the four rectus muscles in the eye sockets were dissected from 5-6 mice [83]. The collected muscles were placed in 0 mM Ca^{2+} Ringer's solution. Excessive connective tissue, tendons, fat, blood clots and vessels were removed as much as possible. After cleanup, the muscles were transferred into the digestion media (DMEM containing 5% FBS, 1% Pen/Strep and 10 mM HEPES) and minced into small blocks using scissors. Collagenase II (Worthington LS004176), dispase II (Sigma D46931G), hyaluronidase (Worthington LS002592) and Dnase I (Worthington LS002139) were added at the final concentration of 0.26%, 0.24%, 0.16% and 0.04%, respectively. The digestion system was placed in an orbital shaker running at 70 rpm at 37 °C for 45 min. The digested muscles were triturated 10 times with a 20-gauge needle attached to a 5 ml syringe. Afterwards the triturated mixture was pipetted onto a pre-wetted 100 µm strainer and centrifuge at 100 g for 2.5 min to precipitate the bulky myofiber debris. The supernatant was transferred onto a pre-wetted 40 um strainer and cells were collected by centrifuged at 1200 g for 6.5 min. The cells were resuspended in sorting media (PBS containing 0.3% BSA, 10 mM HEPES and 1 mM EGTA) and stained with antibodies or dyes at 4 °C for 45 min with shaking. The antibodies used include PE anti-mVcam1 (Biolegend 50604858, 600 ng/10^6 cells), APC anti-mCD31 (Biolegend 50162682, 400 ng/10^6 cells), APC anti-mCD45 (Biolegend 50162782, 400 ng/10^6 cells) APC anti-mSca-1 (Biolegend 50163216, 200 ng/10^6 cells). This antibody combination followed a previous published protocol [40]. Vcam1 is a SC marker, CD31 is a endothelial cell marker, CD45 is a hematopoietic cell marker and Sca-1 is a mesenchymal stem cell marker [40]. For sorting, our target population is $VCAM^+CD31^-CD45^-Sca\text{-}1^-$. When needed, the cells were stained with methyl green (2 µg/ml) to check mortality rate. As a positive control, half of the cells were transferred to a new Eppendorf tube and methanol (precooled at -20°C) was added dropwise with gentle mixing and left on ice for 5 min, the dead cells were wash twice before being mixed with the rest half of cells for methyl green staining. The sorting process was conducted using BD FACS Melody Cell Sorter using a 100 µm nozzle. The excitation laser and emission filter setup for methyl green is the same as APC. The flow rate was tuned between 1-7 to adjust the event rate to 2000-4000/sec. Gating conditions of FSC-A/SSC-A, SSC-H/SSC-W, FSC-H/FSC-W, Vcam1/CD31_CD45_Sca-1 and Vcam1/Methyl green plots were shown in Figure 3-figure supplement 1 and Figure 3-figure supplement 2. The sorted cells were collected in growth media (DMEM containing 20%FBS, 1% Pen/Strep, 1% chick embryonic extract and 10 mM HEPES). Afterwards the cells were seeded into laminin (Corning 354232) -coated plates or glass-bottom dishes containing growth media (without HEPES). Culture media was changed on the third day and the fourth day. To induce differentiation, cells were washed three times with PBS and cultured in differentiation media (DMEM containing 2% horse serum) for 2 more days.

Neuro-muscular coculture assay

For neuromuscular coculture in compartmentalized chambers (XonaCHIPS XC450), XoanCHIPS were coated with poly-L-ornithine (0.5 mg/ml) for 1 hr at 37 °C followed by laminin (0.1 mg/ml) for 1 hr at 37 °C. Primarily cultured satellite cells were seeded at 1x10^5 into the myotube compartment in growth medium for attachment overnight and then switched to differentiation medium and cultured for 2 more days. Afterwards AAV8-CMV-eGFP (Vector Biolabs, 1x10^11 GC/ml) or AAV8-CMV-Cxcl12-IRES-eGFP (Vector Biolabs, 1.5x10^11 GC/ml, the *Cxcl12* gene is of mouse origin) transduction was conducted for one day. The usage of higher titer for the second virus is for matching GFP signal intensity, as IRES-dependent expression is significantly lower than those directly driven by CMV [84]. The chambers were washed with Neurobasal Plus Medium twice before seeding rat spinal motor neurons into the neuronal compartment (1x10^5). The coculture was kept in Neurobasal Plus Medium for 9 more days and half medium change was conducted every 2 days.

For neuromuscular coculture in the same glass-bottom chamber, 8-well chambered cover glasses (Cellvis C8-1.5H-N) were coated with poly-L-ornithine and laminin as described above. Primarily cultured satellite cells were seeded at 1x10^5/chamber in growth medium for attachment overnight and then switched to differentiation medium and cultured for 2 more days. AAV transduction was conducted for one day as described above. The infected myotubes were washed with Neurobasal Plus Medium (Thermo Fisher A3582901, with B-27 and GlutaMax supplement) before the addition of rat spinal motor neurons (4x10^3/chamber, iXCells 10RA-033) to the same chamber. The coculture was kept in Neurobasal Plus Medium for 9 more days and half medium change was conducted every 2 days.

Immunofluorescence (IF) and imaging of whole mount muscle samples

EDL, soleus and EOM (the four rectus muscles) were dissected out and fixed in 4% paraformaldehyde (PFA) for 1 hr. Afterwards the samples were washed with PBS containing 1% glycine once and two more times with PBS. Further fixation and permeabilization was done with methanol at -20°C for 10 min. For diaphragm, the costal muscles and their surrounding rib cages were dissected and immersed in methanol directly for fixation (PFA fixation was skipped because it made the diaphragm harder to flatten and introduced more non-specific noises in staining). The samples were rehydrated and washed with PBS. The epimysium and tendons were removed as much as possible. EDL and soleus were further split into smaller bundles along the longitudinal axis. Then the samples were immersed in blocking buffer (PBS containing 2% BSA, 2% horse serum, 0.1% Tween-20, 0.1% Triton X-100 and 0.05% sodium azide) overnight at 4 °C. Next day the samples were incubated with primary antibodies for 1-2 days. After washing with PBS for three times, the samples were incubated with Alexa Fluor labelled secondary antibodies (Thermo Fisher 1:1000) and Alexa Fluor 488 conjugated α-Bungarotoxin (Thermo Fisher B13422, 1:1000) for 1-2 days. The samples were then washed with PBS, counterstained with DAPI and mounted in antifade mounting media (20 mM Tris, 0.5% N-propyl gallate, 80% glycerol) for imaging. Primary antibodies used: neurofilament (DSHB 2H3 concentrate, 1:250), synaptophysin (Fisher PA11043, 1:400), Pax7 (SCBT sc-81648, 1:100), Pax7 (Thermo Fisher PA1-117, 1:200), CXCL12 (R&D MAB350, 1:200).

To quantify SC number surrounding NMJs, z-stack images were compacted using maximum projection and circles (75 µm in diameter) were drawn around each NMJ in Image J. The DAPI channel was used as a mask to filter out nonspecific staining of Pax7 in the extracellular matrix.

Immunofluorescence and imaging of cultured myoblasts/myotubes and motor neurons

The cells were fixed in 4% PFA for 10 min and then washed with 1% glycine and PBS. Further fixation and permeabilization was done either with methanol at -20°C for 10 min or 0.25% TritonX-100 for 15 min. The samples were then washed with PBS and immersed in blocking buffer for 40 min.

Primary antibody incubation was done at 4 °C overnight. Next day the cells were washed with PBS and incubated with Alexa Fluor labelled secondary antibodies (1:1000) for 2 hours at room temperature, counterstained with DAPI and mounted in antifade mounting media for imaging. Primary antibodies used: Alexa Fluor647 conjugated α-Bungarotoxin (Thermo Fisher B13422, 1:1000), Pax7 (SCBT sc-81648, 1:100), MyoD (SCBT sc-377460, 1:100), Ki-67 (CST 12202S, 1:300), MYH (DSHB MF20 concentrate, 1: 200), neurofilament (DSHB 2H3 concentrate, 1:250), eGFP (Novus NBP-22111AF488, 1:250).

For quantifying innervation ratio, AChR clusters (BTX patches) larger than 10 μm^2 were counted on myotubes that have contact with RSMN neurites. Those myotubes having 0 pixel overlap with RSMN neurites were not included in measurement. The ratio of AChR clusters having overlaps with the RSMN neurites after visual inspection of the whole z-stacks of each view were calculated. The innervation ratio of each view is one dot in the box-and-dot plot in Figure 9C. The measurements were done for 3 rounds of coculture assays.

RNA extraction and qRT-PCR

For cultured SCs, cell culture medium was removed before RNA extraction and Trizol reagent was added to the well before scratching cells off using pipette tips. The homogenate was transferred into tubes containing 5 PRIME Phase Lock Gel (Quantabio 2302830), and 1/10 volume of 1-bromo-3-chloroporpane (Alfa Aesar A11395) was added. The samples were shaken vigorously for 12 s and centrifuged for 15 min at 16,000× *g*. Afterwards, the upper phase was transferred to another Eppendorf tube and isopropanol (1/2 volume of the initial homogenate) was added for precipitation overnight at −20 °C. Next day, after 15 min centrifugation at 16000 *g* the precipitate was washed briefly with 75% ethanol. After another 5 min centrifugation, the ethanol was removed. The precipitate was briefly dried and resuspended in RNase free water. For whole muscle samples, the freshly dissected muscles were snap-frozen in liquid nitrogen, kept at -80 °C freezer overnight and then soaked in RNALater ICE (Thermo Fisher AM7030) for 2-3 days at -20 °C. Before RNA extraction, leftover tendons and neurites were removed and muscles were transferred to 1 ml Trizol. Homogenization was conducted in FastPrep-24 Classic bead beating grinder (MP Biomedicals 116004500). The tissue homogenate was transfer to centrifuge tubes containing phase lock gel (QuantaBio 2302830) and 1/10 volume of 1-bromo-3-chloropropane was added. The tubes were hand shaken for 12 seconds, left at bench top for 2 minutes and then centrifuged at 16000 g at 4 °C for 15 minutes. The upper phase was transferred to a new centrifuge tube and mixed with equal volume of ethanol. The following steps of RNA purification was conducted with Direct-zol RNA Miniprep Plus kit (Zymo Research R2070). RNA concentration was measured with Quantus Fluorometer (Promega E6150). RNA quality was assessed by RNA ScreenTape analysis at Genomics Core Facility at the University of North Texas Health Science Center. Only RNAs with RIN ≥ 9 and 28s/18s ≥ 1 were used for qRT-PCR or RNA-Seq. Reverse transcription was done using Promega GoScript Reverse Transcription system. The qPCR reactions used Maxima SYBR Green/ROX qPCR Master Mix (Thermo Fisher) and were carried out by the StepOnePlus Real-Time PCR system (Thermo Fisher). Relative quantification (RQ) of gene expression was generated by ΔΔCt method. The sequences of primers used for qPCR were listed in Table 1.

Table 1. qPCR primer sequences.

Target gene	Forward primer	Reverse primer
Actn3	AACAGCAGCGGAAAACCTTCA	GGCTTTATTGACATTGGCGATTT
Cxcl12	TGCATCAGTGACGGTAAACCA	TTCTTCAGCCGTGCAACAATC
Gapdh	AGGTCGGTGTGAACGGATTTG	TGTAGACCATGTAGTTGAGGTCA
Hmga2	GAGCCCTCTCCTAAGAGACCC	TTGGCCGTTTTTCTCCAATGG

Notch3	GGTAGTCACTGTGAACACGAGG	CAACTGTCACCAGCATAGCCAG
Scn5a	ATGGCAAACTTCCTGTTACCTC	CCACGGGCTTGTTTTTCAGC

Bulk RNA-Seq and analysis

Non-stranded mRNA sequencing was carried out by BGI Americas Corporation. The average number of clean reads per sample was 45.16 million (ranging from 44.11 to 48.51 million). The average percentage of clean reads was 93.32% (ranging from 92.42% to 93.97%). The average percentage of aligned reads (to Genome Reference Consortium Mouse Build 38 patch release 6) was 96.01% (ranging from 95.40% to 96.67%) and the average percentage of uniquely aligned reads was 86.46% (ranging from 85.12% to 87.63%). To identify differentially expressed genes (DEGs) between different samples (using Poisson distribution method to compare uniquely mapped reads of the gene), only genes with $|\log2FC| \geq 0.4$ and FDR ≤ 0.001 were considered. To identify DEGs between different groups (containing more than one sample, using DESeq2 method), only genes with $|\log2FC| \geq 0.4$ and Qvalue ≤ 0.05 were considered. PCA analysis, hierarchical clustering, functional annotation analysis (KEGG pathway, GO_C, GO_P) were performed in Dr. TOM platform of BGI. Dot plots showing the distribution of activation, differentiation and quiescence signature genes were generated in ggplot2 in R. The BAM files, TPM values will be uploaded to GEO database after acceptance of the manuscript.

Acknowledgement: We thank Dr. Kimberly Bowles at Life Science Core Facility of UT Arlington for the assistance in cell sorting experiments.

Funding: This study has been supported by grants from NIH (R01NS105621 to JZ, R01NS129219 to JZ, JM, LWO, and R01AG071676 To JM and JZ) and the Department of Defense AL170061(W81XWH1810684) to JZ.

References

1. Hardiman, O.; Al-Chalabi, A.; Chio, A.; Corr, E.M.; Logroscino, G.; Robberecht, W.; Shaw, P.J.; Simmons, Z.; van den Berg, L.H. Amyotrophic lateral sclerosis. *Nat Rev Dis Primers* **2017**, *3*, 17071, doi:10.1038/nrdp.2017.71.
2. Vucic, S.; Rothstein, J.D.; Kiernan, M.C. Advances in treating amyotrophic lateral sclerosis: insights from pathophysiological studies. *Trends Neurosci* **2014**, *37*, 433-442, doi:10.1016/j.tins.2014.05.006.
3. Domellöf, F.P. The Extraocular Muscles Are Selectively Spared in ALS. In *Amyotrophic Lateral Sclerosis-Recent Advances and Therapeutic Challenges*; IntechOpen: 2019.
4. Tjust, A.E.; Brännstrom, T.; Pedrosa Domellöf, F. Unaffected motor endplate occupancy in eye muscles of ALS G93A mouse model. *Frontiers in bioscience (Scholar edition)* **2012**, *4*, 1547-1555.
5. Ahmadi, M.; Liu, J.-X.; Brännström, T.; Andersen, P.M.; Stål, P.; Pedrosa-Domellöf, F. Human extraocular muscles in ALS. *Investigative ophthalmology & visual science* **2010**, *51*, 3494-3501.
6. Valdez, G.; Tapia, J.C.; Lichtman, J.W.; Fox, M.A.; Sanes, J.R. Shared resistance to aging and ALS in neuromuscular junctions of specific muscles. *PloS one* **2012**, *7*, e34640.
7. Greaves, L.C.; Yu-Wai-Man, P.; Blakely, E.L.; Krishnan, K.J.; Beadle, N.E.; Kerin, J.; Barron, M.J.; Griffiths, P.G.; Dickinson, A.J.; Turnbull, D.M. Mitochondrial DNA defects and selective extraocular muscle involvement in CPEO. *Investigative ophthalmology & visual science* **2010**, *51*, 3340-3346.
8. Soltys, J.; Gong, B.; Kaminski, H.J.; Zhou, Y.; Kusner, L.L. Extraocular muscle susceptibility to myasthenia gravis: unique immunological environment? *Annals of the New York Academy of Sciences* **2008**, *1132*, 220-224.
9. Luo, G.; Yi, J.; Ma, C.; Xiao, Y.; Yi, F.; Yu, T.; Zhou, J. Defective mitochondrial dynamics is an early event in skeletal muscle of an amyotrophic lateral sclerosis mouse model. *PLoS One* **2013**, *8*, e82112, doi:10.1371/journal.pone.0082112.
10. Yi, J.; Li, A.; Li, X.; Park, K.; Zhou, X.; Yi, F.; Xiao, Y.; Yoon, D.; Tan, T.; Ostrow, L.W.; et al. MG53 Preserves Neuromuscular Junction Integrity and Alleviates ALS Disease Progression. *Antioxidants (Basel)* **2021**, *10*, doi:10.3390/antiox10101522.
11. Zhou, J.; Li, A.; Li, X.; Yi, J. Dysregulated mitochondrial Ca(2+) and ROS signaling in skeletal muscle of ALS mouse model. *Arch Biochem Biophys* **2019**, *663*, 249-258, doi:10.1016/j.abb.2019.01.024.
12. Zhou, J.; Yi, J.; Fu, R.; Liu, E.; Siddique, T.; Rios, E.; Deng, H.X. Hyperactive intracellular calcium signaling associated with localized mitochondrial defects in skeletal muscle of an animal model of amyotrophic lateral sclerosis. *J Biol Chem* **2010**, *285*, 705-712, doi:10.1074/jbc.M109.041319.
13. Xiao, Y.; Ma, C.; Yi, J.; Wu, S.; Luo, G.; Xu, X.; Lin, P.H.; Sun, J.; Zhou, J. Suppressed autophagy flux in skeletal muscle of an amyotrophic lateral sclerosis mouse model during disease progression. *Physiol Rep* **2015**, *3*, doi:10.14814/phy2.12271.
14. Xiao, Y.; Karam, C.; Yi, J.; Zhang, L.; Li, X.; Yoon, D.; Wang, H.; Dhakal, K.; Ramlow, P.; Yu, T.; et al. ROS-related mitochondrial dysfunction in skeletal muscle of an ALS mouse model during the disease progression. *Pharmacol Res* **2018**, *138*, 25-36, doi:10.1016/j.phrs.2018.09.008.
15. Dobrowolny, G.; Aucello, M.; Rizzuto, E.; Beccafico, S.; Mammucari, C.; Boncompagni, S.; Belia, S.; Wannenes, F.; Nicoletti, C.; Del Prete, Z.; et al. Skeletal muscle is a primary target of SOD1G93A-mediated toxicity. *Cell metabolism* **2008**, *8*, 425-436, doi:10.1016/j.cmet.2008.09.002.
16. Wong, M.; Martin, L.J. Skeletal muscle-restricted expression of human SOD1 causes motor neuron degeneration in transgenic mice. *Hum Mol Genet* **2010**, *19*, 2284-2302, doi:10.1093/hmg/ddq106.
17. Loeffler, J.P.; Picchiarelli, G.; Dupuis, L.; Gonzalez De Aguilar, J.L. The Role of Skeletal Muscle in Amyotrophic Lateral Sclerosis. *Brain Pathol* **2016**, *26*, 227-236, doi:10.1111/bpa.12350.
18. Dadon-Nachum, M.; Melamed, E.; Offen, D. The "dying-back" phenomenon of motor neurons in ALS. *J Mol Neurosci* **2011**, *43*, 470-477, doi:10.1007/s12031-010-9467-1.
19. Fischer, L.R.; Culver, D.G.; Tennant, P.; Davis, A.A.; Wang, M.; Castellano-Sanchez, A.; Khan, J.; Polak, M.A.; Glass, J.D. Amyotrophic lateral sclerosis is a distal axonopathy: evidence in mice and man. *Exp Neurol* **2004**, *185*, 232-240, doi:10.1016/j.expneurol.2003.10.004.

634 20. Frey, D.; Schneider, C.; Xu, L.; Borg, J.; Spooren, W.; Caroni, P. Early and selective loss of neuromuscular
635 synapse subtypes with low sprouting competence in motoneuron diseases. *J Neurosci* **2000**, *20*, 2534-
636 2542, doi:10.1523/JNEUROSCI.20-07-02534.2000.
637 21. Campanari, M.L.; Bourefis, A.R.; Kabashi, E. Diagnostic Challenge and Neuromuscular Junction
638 Contribution to ALS Pathogenesis. *Front Neurol* **2019**, *10*, 68, doi:10.3389/fneur.2019.00068.
639 22. Cappello, V.; Francolini, M. Neuromuscular Junction Dismantling in Amyotrophic Lateral Sclerosis. *Int J*
640 *Mol Sci* **2017**, *18*, doi:10.3390/ijms18102092.
641 23. Clark, J.A.; Southam, K.A.; Blizzard, C.A.; King, A.E.; Dickson, T.C. Axonal degeneration, distal collateral
642 branching and neuromuscular junction architecture alterations occur prior to symptom onset in the
643 SOD1(G93A) mouse model of amyotrophic lateral sclerosis. *J Chem Neuroanat* **2016**, *76*, 35-47,
644 doi:10.1016/j.jchemneu.2016.03.003.
645 24. Martineau, E.; Di Polo, A.; Vande Velde, C.; Robitaille, R. Dynamic neuromuscular remodeling precedes
646 motor-unit loss in a mouse model of ALS. *Elife* **2018**, *7*, doi:10.7554/eLife.41973.
647 25. Horn, A.K.E.; Straka, H. Functional Organization of Extraocular Motoneurons and Eye Muscles. *Annu*
648 *Rev Vis Sci* **2021**, *7*, 793-825, doi:10.1146/annurev-vision-100119-125043.
649 26. Nijssen, J.; Comley, L.H.; Hedlund, E. Motor neuron vulnerability and resistance in amyotrophic lateral
650 sclerosis. *Acta Neuropathol* **2017**, *133*, 863-885, doi:10.1007/s00401-017-1708-8.
651 27. Ince, P.; Stout, N.; Shaw, P.; Slade, J.; Hunziker, W.; Heizmann, C.W.; Baimbridge, K.G. Parvalbumin and
652 calbindin D-28k in the human motor system and in motor neuron disease. *Neuropathol Appl Neurobiol*
653 **1993**, *19*, 291-299, doi:10.1111/j.1365-2990.1993.tb00443.x.
654 28. Alexianu, M.E.; Ho, B.K.; Mohamed, A.H.; La Bella, V.; Smith, R.G.; Appel, S.H. The role of calcium-
655 binding proteins in selective motoneuron vulnerability in amyotrophic lateral sclerosis. *Ann Neurol*
656 **1994**, *36*, 846-858, doi:10.1002/ana.410360608.
657 29. Mosier, D.R.; Siklos, L.; Appel, S.H. Resistance of extraocular motoneuron terminals to effects of
658 amyotrophic lateral sclerosis sera. *Neurology* **2000**, *54*, 252-255, doi:10.1212/wnl.54.1.252.
659 30. Fischer, M.D.; Gorospe, J.R.; Felder, E.; Bogdanovich, S.; Pedrosa-Domellof, F.; Ahima, R.S.; Rubinstein,
660 N.A.; Hoffman, E.P.; Khurana, T.S. Expression profiling reveals metabolic and structural components of
661 extraocular muscles. *Physiol Genomics* **2002**, *9*, 71-84, doi:10.1152/physiolgenomics.00115.2001.
662 31. Harandi, V.M.; Lindquist, S.; Kolan, S.S.; Brännström, T.; Liu, J.-X. Analysis of neurotrophic factors in
663 limb and extraocular muscles of mouse model of amyotrophic lateral sclerosis. *PLoS One* **2014**, *9*,
664 e109833.
665 32. Harandi, V.M.; Gaied, A.R.; Brännström, T.; Domellöf, F.P.; Liu, J.-X. Unchanged neurotrophic factors
666 and their receptors correlate with sparing in extraocular muscles in amyotrophic lateral sclerosis.
667 *Investigative ophthalmology & visual science* **2016**, *57*, 6831-6842.
668 33. Liu, W.; Wei-LaPierre, L.; Klose, A.; Dirksen, R.T.; Chakkalakal, J.V. Inducible depletion of adult skeletal
669 muscle stem cells impairs the regeneration of neuromuscular junctions. *elife* **2015**, *4*, e09221.
670 34. Liu, W.; Klose, A.; Forman, S.; Paris, N.D.; Wei-LaPierre, L.; Cortes-Lopez, M.; Tan, A.; Flaherty, M.;
671 Miura, P.; Dirksen, R.T. Loss of adult skeletal muscle stem cells drives age-related neuromuscular
672 junction degeneration. *Elife* **2017**, *6*, e26464.
673 35. Stuelsatz, P.; Shearer, A.; Li, Y.; Muir, L.A.; Ieronimakis, N.; Shen, Q.W.; Kirillova, I.; Yablonka-Reuveni,
674 Z. Extraocular muscle satellite cells are high performance myo-engines retaining efficient regenerative
675 capacity in dystrophin deficiency. *Developmental biology* **2015**, *397*, 31-44.
676 36. Zhang, Y.G.; Wu, S.; Yi, J.; Xia, Y.; Jin, D.; Zhou, J.; Sun, J. Target Intestinal Microbiota to Alleviate
677 Disease Progression in Amyotrophic Lateral Sclerosis. *Clin Ther* **2017**,
678 doi:10.1016/j.clinthera.2016.12.014.
679 37. Sekiguchi, K.; Kanda, F.; Mitsui, S.; Kohara, N.; Chihara, K. Fibrillation potentials of denervated rat
680 skeletal muscle are associated with expression of cardiac-type voltage-gated sodium channel isoform
681 Nav1. 5. *Clinical neurophysiology* **2012**, *123*, 1650-1655.

682 38. Rowan, S.L.; Rygiel, K.; Purves-Smith, F.M.; Solbak, N.M.; Turnbull, D.M.; Hepple, R.T. Denervation
683 causes fiber atrophy and myosin heavy chain co-expression in senescent skeletal muscle. *PLoS One*
684 **2012**, *7*, e29082, doi:10.1371/journal.pone.0029082.
685 39. Carreras, D.; Martinez-Moreno, R.; Pinsach-Abuin, M.l.; Santafe, M.M.; Gomà, P.; Brugada, R.; Scornik,
686 F.S.; Perez, G.J.; Pagans, S. Epigenetic changes governing Scn5a expression in denervated skeletal
687 muscle. *International journal of molecular sciences* **2021**, *22*, 2755.
688 40. Liu, L.; Cheung, T.H.; Charville, G.W.; Rando, T.A. Isolation of skeletal muscle stem cells by
689 fluorescence-activated cell sorting. *Nature protocols* **2015**, *10*, 1612-1624.
690 41. Metzger, J.M.; Scheidt, K.; Fitts, R.H. Histochemical and physiological characteristics of the rat
691 diaphragm. *Journal of applied physiology* **1985**, *58*, 1085-1091.
692 42. Rochester, D.F. The diaphragm: contractile properties and fatigue. *The Journal of clinical investigation*
693 **1985**, *75*, 1397-1402.
694 43. Polla, B.; D'Antona, G.; Bottinelli, R.; Reggiani, C. Respiratory muscle fibres: specialisation and
695 plasticity. *Thorax* **2004**, *59*, 808-817.
696 44. Augusto, V.; Padovani, C.R.; Campos, G.E.R. Skeletal muscle fiber types in C57BL6J mice. *Journal of*
697 *Morphological Sciences* **2017**, *21*, 0-0.
698 45. Prieto, D.; Aparicio, G.; Morande, P.E.; Zolessi, F.R. A fast, low cost, and highly efficient fluorescent
699 DNA labeling method using methyl green. *Histochemistry and cell biology* **2014**, *142*, 335-345.
700 46. Ribeiro, A.F., Jr.; Souza, L.S.; Almeida, C.F.; Ishiba, R.; Fernandes, S.A.; Guerrieri, D.A.; Santos, A.L.F.;
701 Onofre-Oliveira, P.C.G.; Vainzof, M. Muscle satellite cells and impaired late stage regeneration in
702 different murine models for muscular dystrophies. *Sci Rep* **2019**, *9*, 11842, doi:10.1038/s41598-019-
703 48156-7.
704 47. Ancel, S.; Stuelsatz, P.; Feige, J.N. Muscle stem cell quiescence: controlling stemness by staying asleep.
705 *Trends in Cell Biology* **2021**, *31*, 556-568.
706 48. Iezzi, S.; Cossu, G.; Nervi, C.; Sartorelli, V.; Puri, P.L. Stage-specific modulation of skeletal myogenesis
707 by inhibitors of nuclear deacetylases. *Proceedings of the National Academy of Sciences* **2002**, *99*, 7757-
708 7762.
709 49. Fukada, S.-i.; Uezumi, A.; Ikemoto, M.; Masuda, S.; Segawa, M.; Tanimura, N.; Yamamoto, H.; Miyagoe-
710 Suzuki, Y.; Takeda, S.i. Molecular signature of quiescent satellite cells in adult skeletal muscle. *Stem*
711 *cells* **2007**, *25*, 2448-2459.
712 50. Fujimaki, S.; Seko, D.; Kitajima, Y.; Yoshioka, K.; Tsuchiya, Y.; Masuda, S.; Ono, Y. Notch1 and Notch2
713 coordinately regulate stem cell function in the quiescent and activated states of muscle satellite cells.
714 *Stem Cells* **2018**, *36*, 278-285.
715 51. Mourikis, P.; Sambasivan, R.; Castel, D.; Rocheteau, P.; Bizzarro, V.; Tajbakhsh, S. A critical requirement
716 for notch signaling in maintenance of the quiescent skeletal muscle stem cell state. *Stem cells* **2012**,
717 *30*, 243-252.
718 52. Bröhl, D.; Vasyutina, E.; Czajkowski, M.T.; Griger, J.; Rassek, C.; Rahn, H.-P.; Purfürst, B.; Wende, H.;
719 Birchmeier, C. Colonization of the satellite cell niche by skeletal muscle progenitor cells depends on
720 Notch signals. *Developmental cell* **2012**, *23*, 469-481.
721 53. Schmidt, K.; Glaser, G.; Wernig, A.; Wegner, M.; Rosorius, O. Sox8 is a specific marker for muscle
722 satellite cells and inhibits myogenesis. *Journal of Biological Chemistry* **2003**, *278*, 29769-29775.
723 54. Negro, S.; Lessi, F.; Duregotti, E.; Aretini, P.; La Ferla, M.; Franceschi, S.; Menicagli, M.; Bergamin, E.;
724 Radice, E.; Thelen, M. CXCL 12α/SDF-1 from perisynaptic Schwann cells promotes regeneration of
725 injured motor axon terminals. *EMBO molecular medicine* **2017**, *9*, 1000-1010.
726 55. Arnett, A.L.; Konieczny, P.; Ramos, J.N.; Hall, J.; Odom, G.; Yablonka-Reuveni, Z.; Chamberlain, J.R.;
727 Chamberlain, J.S. Adeno-associated viral vectors do not efficiently target muscle satellite cells.
728 *Molecular Therapy-Methods & Clinical Development* **2014**, *1*.
729 56. Ellis, B.L.; Hirsch, M.L.; Barker, J.C.; Connelly, J.P.; Steininger, R.J.; Porteus, M.H. A survey of ex vivo/in
730 vitro transduction efficiency of mammalian primary cells and cell lines with Nine natural adeno-

731 associated virus (AAV1-9) and one engineered adeno-associated virus serotype. *Virology journal* **2013**,
732 *10*, 1-10.
733 57. Bebelman, M.P.; Bun, P.; Huveneers, S.; van Niel, G.; Pegtel, D.M.; Verweij, F.J. Real-time imaging of
734 multivesicular body–plasma membrane fusion to quantify exosome release from single cells. *Nature*
735 *protocols* **2020**, *15*, 102-121.
736 58. Dent, E.W.; Barnes, A.M.; Tang, F.; Kalil, K. Netrin-1 and semaphorin 3A promote or inhibit cortical
737 axon branching, respectively, by reorganization of the cytoskeleton. *Journal of Neuroscience* **2004**, *24*,
738 3002-3012.
739 59. Fukunishi, A.; Maruyama, T.; Zhao, H.; Tiwari, M.; Kang, S.; Kumanogoh, A.; Yamamoto, N. The action
740 of Semaphorin7A on thalamocortical axon branching. *Journal of neurochemistry* **2011**, *118*, 1008-1015.
741 60. Jeroen Pasterkamp, R.; Peschon, J.J.; Spriggs, M.K.; Kolodkin, A.L. Semaphorin 7A promotes axon
742 outgrowth through integrins and MAPKs. *Nature* **2003**, *424*, 398-405.
743 61. Tang, F.; Kalil, K. Netrin-1 induces axon branching in developing cortical neurons by frequency-
744 dependent calcium signaling pathways. *Journal of Neuroscience* **2005**, *25*, 6702-6715.
745 62. Hayano, Y.; Sasaki, K.; Ohmura, N.; Takemoto, M.; Maeda, Y.; Yamashita, T.; Hata, Y.; Kitada, K.;
746 Yamamoto, N. Netrin-4 regulates thalamocortical axon branching in an activity-dependent fashion.
747 *Proceedings of the National Academy of Sciences* **2014**, *111*, 15226-15231.
748 63. Dong, F.; Liu, Y.; Yan, W.; Meng, Q.; Song, X.; Cheng, B.; Yao, R. Netrin-4: Focus on Its Role in Axon
749 Guidance, Tissue Stability, Angiogenesis and Tumors. *Cellular and Molecular Neurobiology* **2023**, *43*,
750 1663-1683.
751 64. McLoon, L.K.; Wirtschafter, J. Activated satellite cells are present in uninjured extraocular muscles of
752 mature mice. *Transactions of the American Ophthalmological Society* **2002**, *100*, 119.
753 65. Ishimoto, S.; Goto, I.; Ohta, M.; Kuroiwa, Y. A quantitative study of the muscle satellite cells in various
754 neuromuscular disorders. *Journal of the neurological sciences* **1983**, *62*, 303-314.
755 66. Pradat, P.-F.; Barani, A.; Wanschitz, J.; Dubourg, O.; Lombes, A.; Bigot, A.; Mouly, V.; Bruneteau, G.;
756 Salachas, F.; Lenglet, T. Abnormalities of satellite cells function in amyotrophic lateral sclerosis.
757 *Amyotrophic Lateral Sclerosis* **2011**, *12*, 264-271.
758 67. Scaramozza, A.; Marchese, V.; Papa, V.; Salaroli, R.; Soraru, G.; Angelini, C.; Cenacchi, G. Skeletal
759 muscle satellite cells in amyotrophic lateral sclerosis. *Ultrastructural pathology* **2014**, *38*, 295-302.
760 68. Manzano, R.; Toivonen, J.M.; Calvo, A.C.; Oliván, S.; Zaragoza, P.; Muñoz, M.J.; Montarras, D.; Osta, R.
761 Quantity and activation of myofiber-associated satellite cells in a mouse model of amyotrophic lateral
762 sclerosis. *Stem Cell Reviews and Reports* **2012**, *8*, 279-287.
763 69. Manzano, R.; Toivonen, J.M.; Calvo, A.C.; Oliván, S.; Zaragoza, P.; Rodellar, C.; Montarras, D.; Osta, R.
764 Altered in vitro proliferation of mouse SOD1-G93A skeletal muscle satellite cells. *Neurodegenerative*
765 *Diseases* **2013**, *11*, 153-164.
766 70. Lieberam, I.; Agalliu, D.; Nagasawa, T.; Ericson, J.; Jessell, T.M. A Cxcl12-CXCR4 chemokine signaling
767 pathway defines the initial trajectory of mammalian motor axons. *Neuron* **2005**, *47*, 667-679.
768 71. Whitman, M.C.; Nguyen, E.H.; Bell, J.L.; Tenney, A.P.; Gelber, A.; Engle, E.C. Loss of CXCR4/CXCL12
769 signaling causes oculomotor nerve misrouting and development of motor trigeminal to oculomotor
770 synkinesis. *Investigative ophthalmology & visual science* **2018**, *59*, 5201-5209.
771 72. Griffin, C.A.; Apponi, L.H.; Long, K.K.; Pavlath, G.K. Chemokine expression and control of muscle cell
772 migration during myogenesis. *Journal of cell science* **2010**, *123*, 3052-3060.
773 73. Brzoska, E.; Kowalewska, M.; Markowska-Zagrajek, A.; Kowalski, K.; Archacka, K.; Zimowska, M.;
774 Grabowska, I.; Czerwińska, A.M.; Czarnecka-Góra, M.; Stremińska, W. Sdf-1 (CXCL12) improves
775 skeletal muscle regeneration via the mobilisation of Cxcr4 and CD34 expressing cells. *Biology of the*
776 *Cell* **2012**, *104*, 722-737.
777 74. Davie, J.R. Inhibition of histone deacetylase activity by butyrate. *The Journal of nutrition* **2003**, *133*,
778 2485S-2493S.

75. Sincennes, M.-C.; Brun, C.E.; Rudnicki, M.A. Concise review: epigenetic regulation of myogenesis in health and disease. *Stem cells translational medicine* **2016**, *5*, 282-290.
76. Moresi, V.; Marroncelli, N.; Adamo, S. New insights into the epigenetic control of satellite cells. *World journal of stem cells* **2015**, *7*, 945.
77. Johnston, L.A.; Tapscott, S.J.; Eisen, H. Sodium butyrate inhibits myogenesis by interfering with the transcriptional activation function of MyoD and myogenin. *Molecular and cellular biology* **1992**.
78. Donohoe, D.R.; Garge, N.; Zhang, X.; Sun, W.; O'Connell, T.M.; Bunger, M.K.; Bultman, S.J. The microbiome and butyrate regulate energy metabolism and autophagy in the mammalian colon. *Cell metabolism* **2011**, *13*, 517-526, doi:10.1016/j.cmet.2011.02.018.
79. Li, A.; Li, X.; Yi, J.; Ma, J.; Zhou, J. Butyrate Feeding Reverses CypD-Related Mitoflash Phenotypes in Mouse Myofibers. *Int J Mol Sci* **2021**, *22*, doi:10.3390/ijms22147412.
80. Li, X.; Dong, L.; Li, A.; Yi, J.; Brotto, M.; Zhou, J. Butyrate Ameliorates Mitochondrial Respiratory Capacity of The Motor-Neuron-like Cell Line NSC34-G93A, a Cellular Model for ALS. *Biomolecules* **2022**, *12*, doi:10.3390/biom12020333.
81. Paganoni, S.; Macklin, E.A.; Hendrix, S.; Berry, J.D.; Elliott, M.A.; Maiser, S.; Karam, C.; Caress, J.B.; Owegi, M.A.; Quick, A. Trial of sodium phenylbutyrate–taurursodiol for amyotrophic lateral sclerosis. *New England Journal of Medicine* **2020**, *383*, 919-930.
82. Gurney, M.E.; Pu, H.; Chiu, A.Y.; Dal Canto, M.C.; Polchow, C.Y.; Alexander, D.D.; Caliendo, J.; Hentati, A.; Kwon, Y.W.; Deng, H.-X. Motor neuron degeneration in mice that express a human Cu, Zn superoxide dismutase mutation. *Science* **1994**, *264*, 1772-1775.
83. Eckhardt, J.; Bachmann, C.; Sekulic-Jablanovic, M.; Enzmann, V.; Park, K.H.; Ma, J.; Takeshima, H.; Zorzato, F.; Treves, S. Extraocular muscle function is impaired in ryr3−/− mice. *Journal of general physiology* **2019**, *151*, 929-943.
84. Mizuguchi, H.; Xu, Z.; Ishii-Watabe, A.; Uchida, E.; Hayakawa, T. IRES-dependent second gene expression is significantly lower than cap-dependent first gene expression in a bicistronic vector. *Molecular Therapy* **2000**, *1*, 376-382.

Figures and figure legends

Figure 1

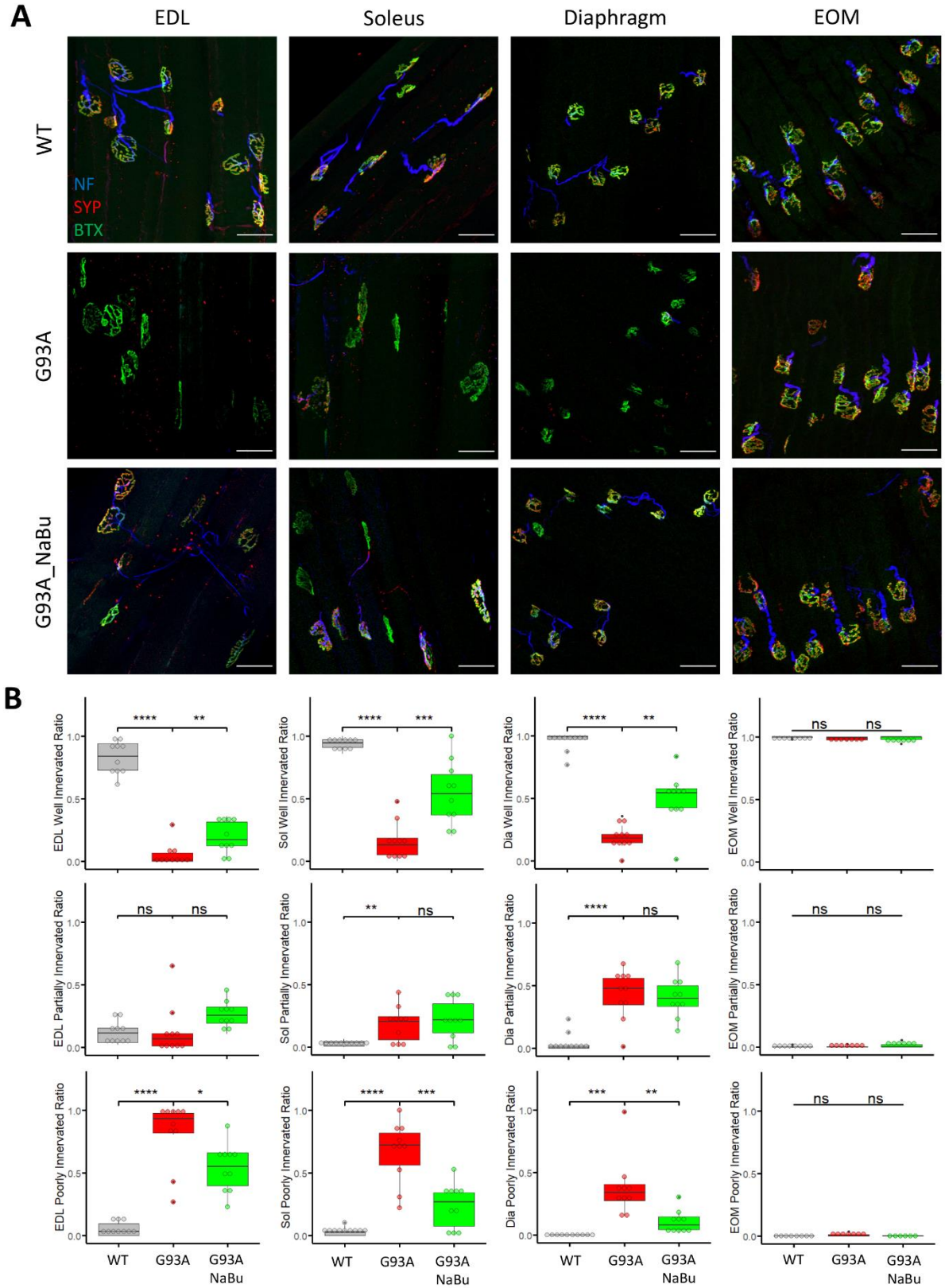

Figure 1. Characterizing NMJ integrity in muscles dissected from wild-type controls and end-stage G93A mice with or without NaBu feeding. (**A**) Representative compacted z-stack scan images of whole-mount EDL, soleus diaphragm extraocular muscles stained with antibodies against neurofilament medium chain (NF, labeling axons), synaptophysin (SYP, labeling axon terminals) and Alexa Fluor 488 conjugated α-Bungarotoxin (BTX, labeling AChRs on muscle membrane). scale bars, 50 μm. **(B)** Mean ratios of well innervated NMJs (SYP signals are present in >60% of BTX positive area), partially innervated NMJs (SYP signals are present in 30-60% of BTX positive area) and poorly innervated NMJs (SYP signals are present in <30% of BTX positive area) and in different types of muscles dissected from WT controls and end-stage G93A mice with or without NaBu feeding (tens to hundreds of NMJs were measured per muscle type per mice, also see Figure 1-figure supplement 1 and Figure 1-table supplement 1). * $P < 0.05$; ** $P < 0.01$; **** $P < 0.0001$; ns, not significant.

Figure 2

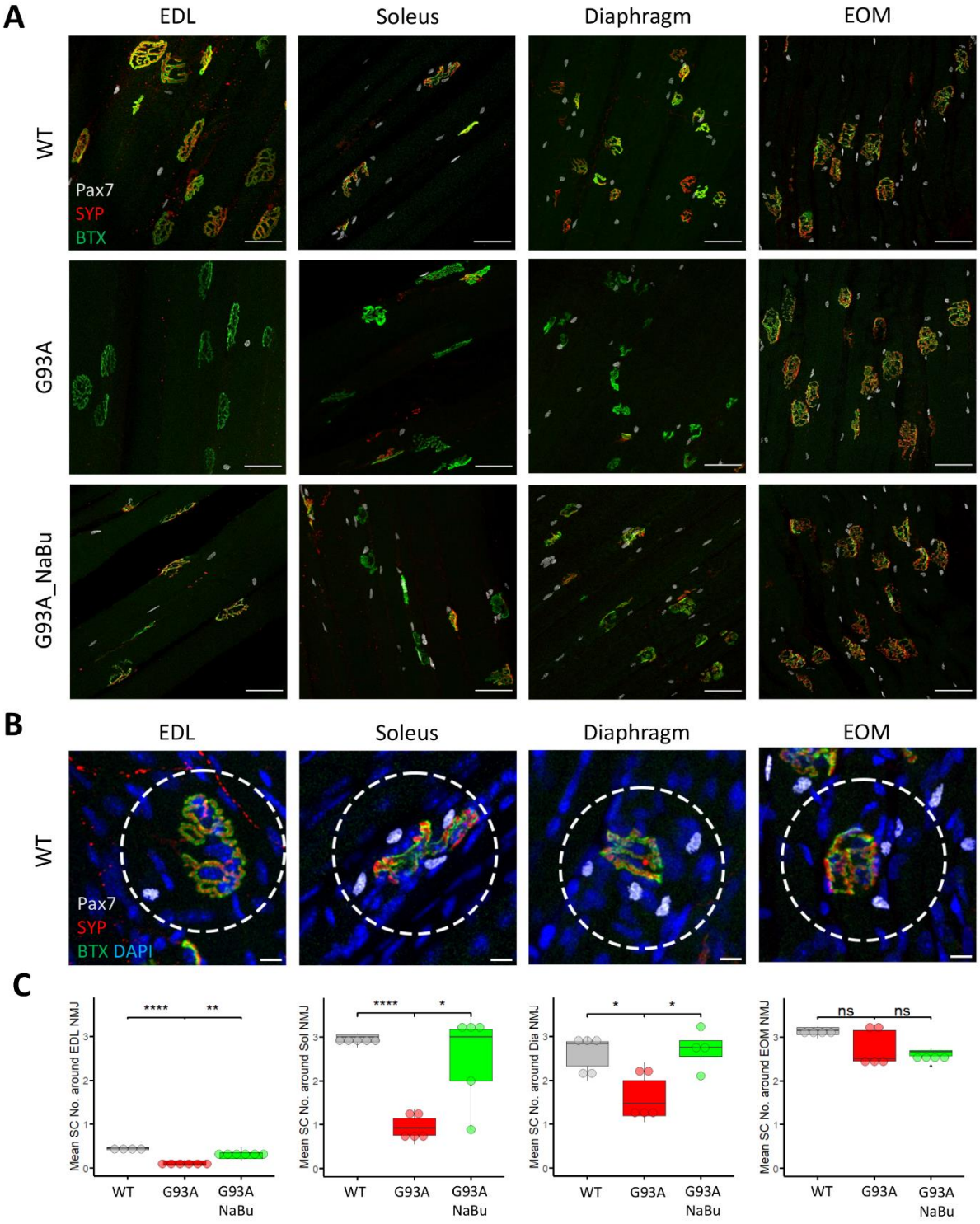
A
EDL
Soleus
Diaphragm
EOM
WT
G93A
G93A_NaBu
Pax7
SYP
BTX
B
EDL
Soleus
Diaphragm
EOM
WT
Pax7
SYP
BTX DAPI
C
Mean SC No. around EDL NMJ
Mean SC No. around Sol NMJ
Mean SC No. around Dia NMJ
Mean SC No. around EOM NMJ
****
**
*
ns
WT
G93A
G93A NaBu

Figure 2. Quantification of peri-NMJ SC abundance in muscles dissected from wild-type controls and end-stage G93A mice with or without NaBu feeding. (**A**) Representative compacted z-stack scan images of whole-mount EDL, soleus diaphragm extraocular muscles stained with antibodies against Pax7 (labeling SCs), SYP and BTX-Alexa Fluor 488. scale bars, 50 μm. (**B**) To measure the abundance of SCs around NMJs, circles of 75 μm diameter were drawn around the NMJs and the number of nuclear $Pax7^{+}$ cells (co-localized with DAPI) were counted. Scale bars, 10 μm. (**C**) Mean number of SCs around NMJs in different types of muscles dissected from WT controls and end-stage G93A mice with or without NaBu feeding (tens to hundreds of NMJs were measured per muscle type per mice, see Figure 2-table supplement 1). * $P < 0.05$; ** $P < 0.01$; **** $P < 0.0001$; ns, not significant.

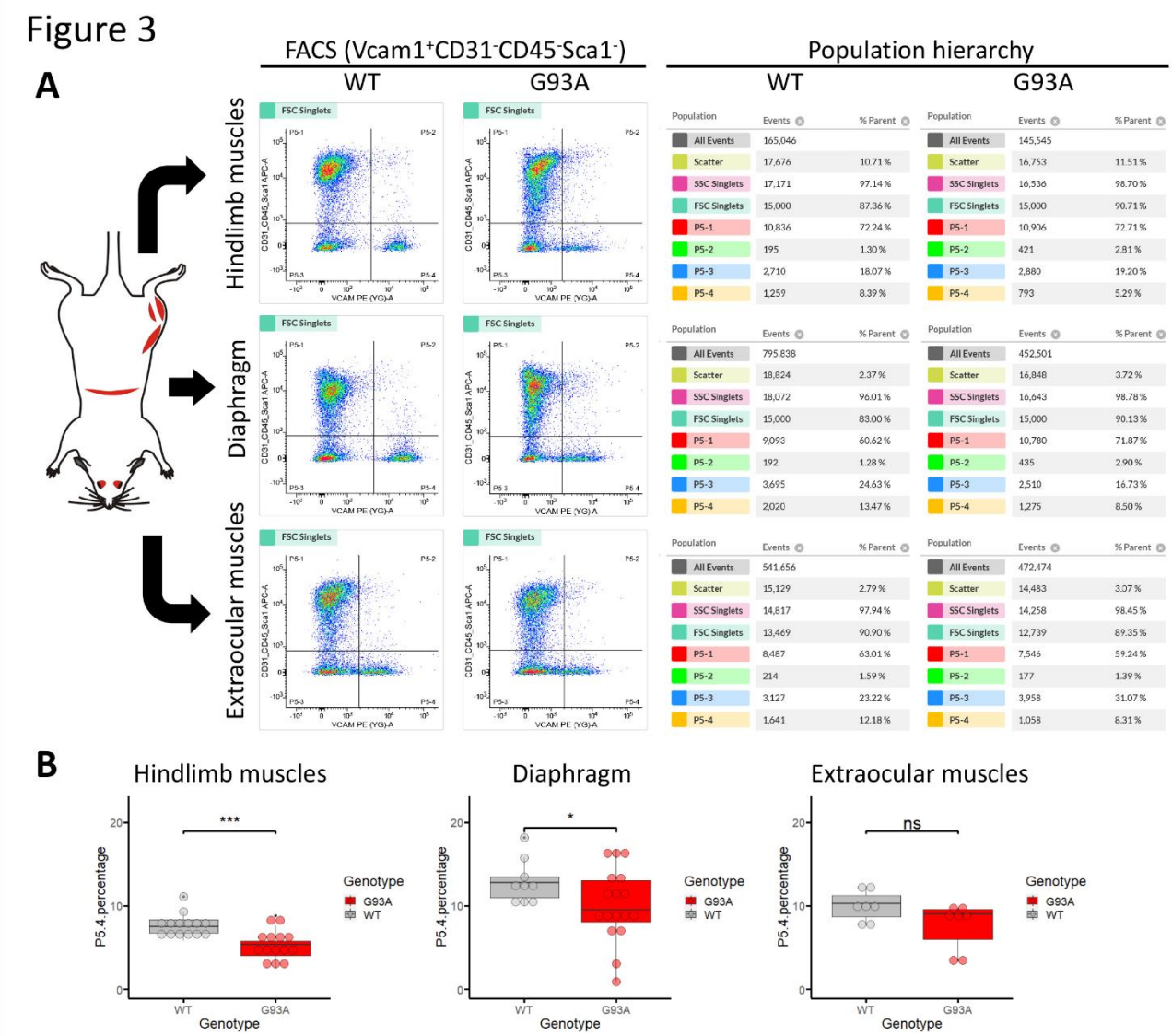

Figure 3. Isolation of SCs from wildtype and G93A muscles using fluorescence activated cell sorting. (**A**) Representative FACS profiles during the isolation of Vcam1^{+}CD31^{-}CD45^{-}Sca1^{-} cells (gate P5-4). The corresponding population hierarchies are shown right to the plots. For single antibody staining controls, unstained controls and viability test, see Figure 3-figure supplement 1 and Figure 3-figure supplement 2. (**B**) Comparing the percentage of events in the P5-4 gate between cells isolated from WT and G93A mice. * $P < 0.05$; *** $P < 0.001$; ns: not significant.

Figure 4

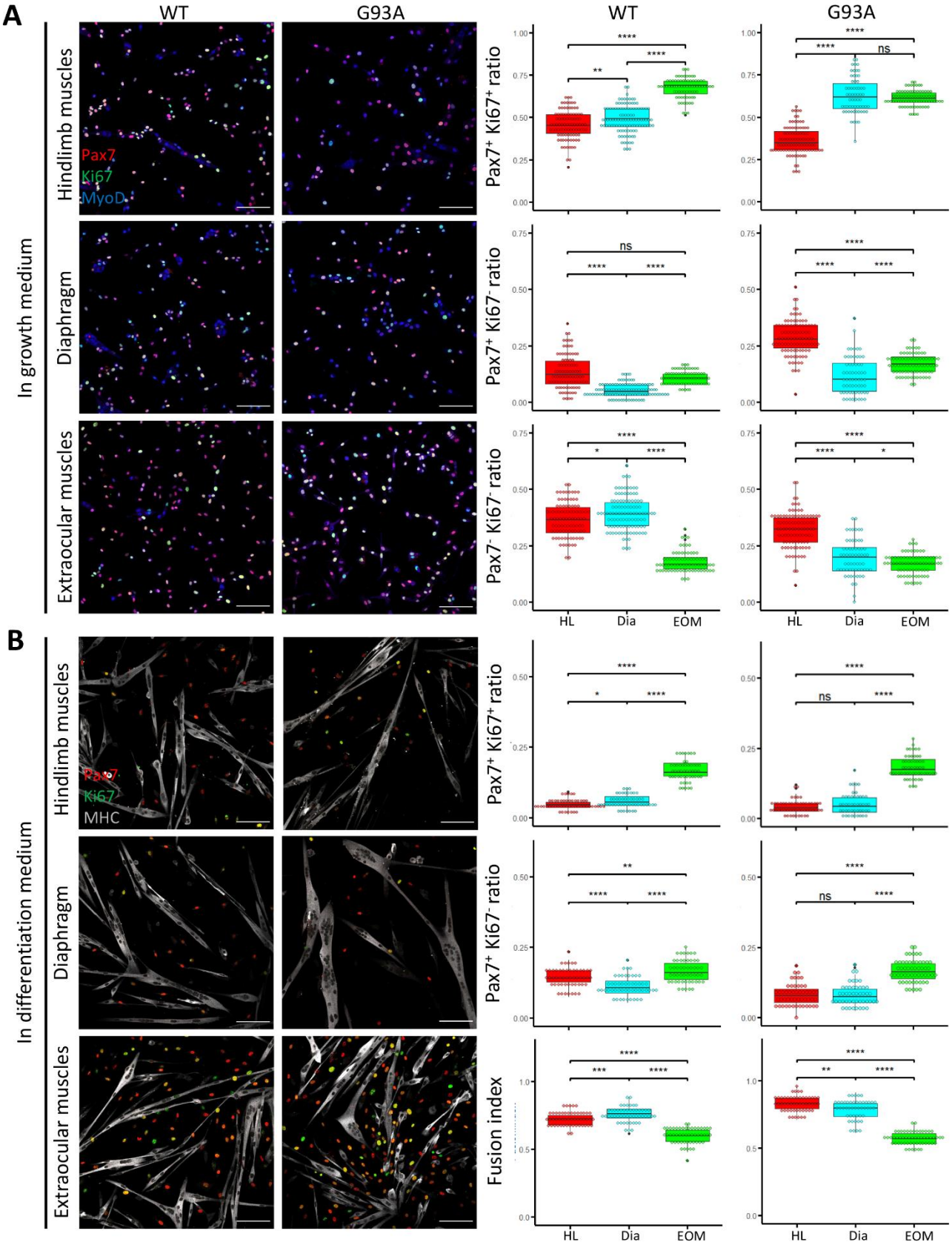
A
WT
G93A
WT
G93A
In growth medium
Hindlimb muscles
Diaphragm
Extraocular muscles
Pax7
Ki67
MyoD
Pax7+ Ki67+ ratio
Pax7+ Ki67- ratio
Pax7- Ki67- ratio
HL
Dia
EOM
B
In differentiation medium
Hindlimb muscles
Diaphragm
Extraocular muscles
Pax7
Ki67
MHC
Pax7+ Ki67+ ratio
Pax7+ Ki67- ratio
Fusion index
HL
Dia
EOM

873

Figure 4. Proliferation and differentiation properties of FACS-isolated SCs in culture. (**A**) Representative images of FACS-isolated SCs cultured for 4 days in growth medium stained with antibodies against Pax7, Ki67 (proliferating cell marker), MyoD (myogenic lineage marker). Measurement results for the ratios of $Pax7^{+}Ki67^{+}$, $Pax7^{+}Ki67^{-}$ and $Pax7^{-}Ki67^{-}$ cells are shown in the right two panels. Scale bars, 100 μm. * $P < 0.05$; ** $P < 0.01$; **** $P < 0.0001$; ns, not significant. (**B**) Representative images of FACS-isolated SCs cultured for 4 days in growth medium and 2 days in differentiation medium stained with antibodies against Pax7, Ki67, myosin heavy chain (MHC, differentiated myotube marker). Measurement results for the ratios of $Pax7^{+}Ki67^{+}$ and $Pax7^{+}Ki67^{-}$ cells, as well as the fusion indices are shown in the right two panels.

Figure 5

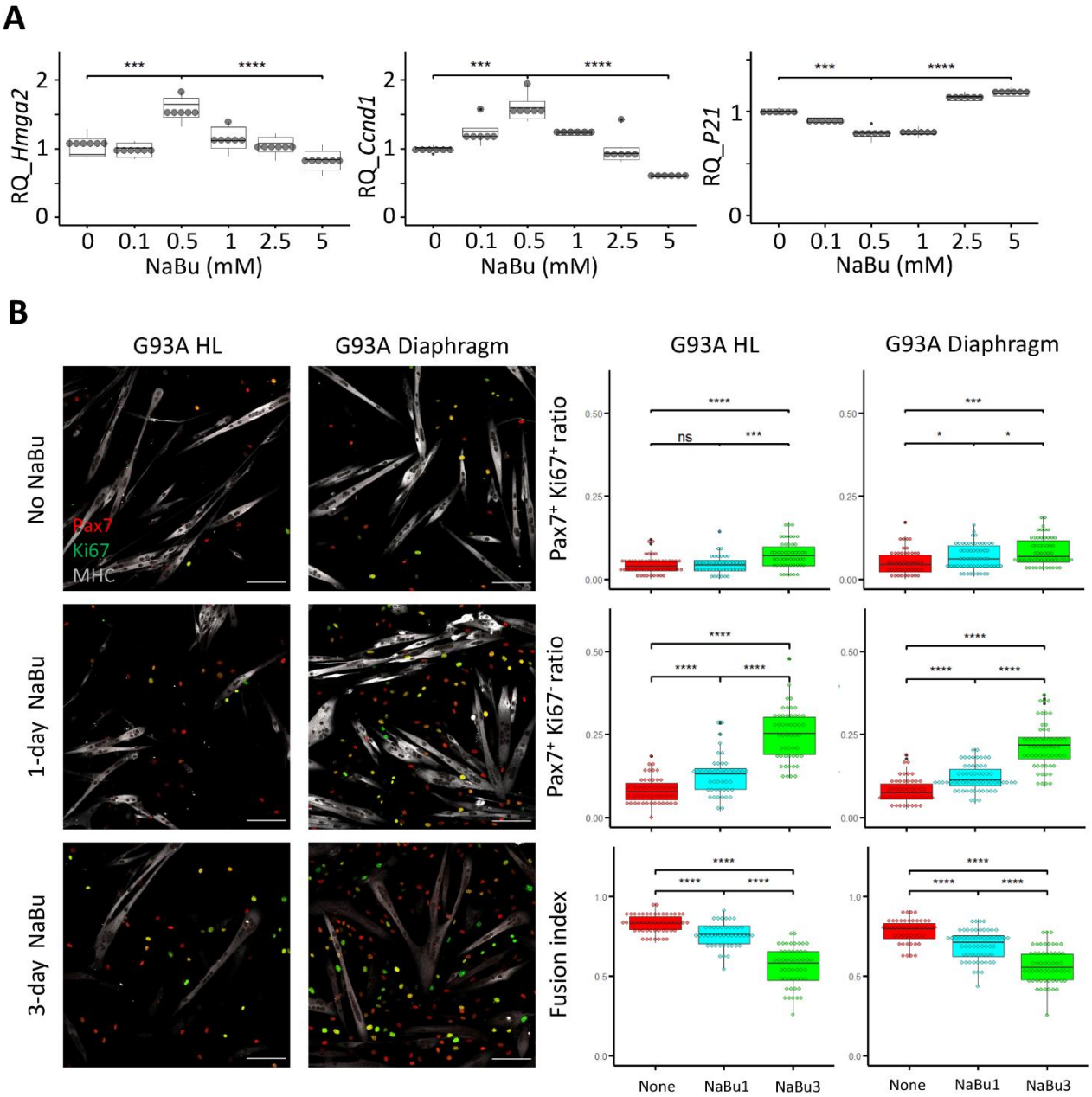

Figure 5. Proliferation and differentiation properties of FACS-isolated SCs with different NaBu treatment conditions. (**A**) qRT-PCR based relative quantification of *Hmga2*, *Ccnd1* and *P21* expression in FACS-isolated G93A HL SCs cultured with different doses of NaBu in growth medium for 1 day (n = 6). *** P < 0.001; **** P < 0.0001. (**B**) Left two panels show the representative images of FACS-isolated G93A HL and diaphragm SCs cultured in growth medium for 4 days and differentiation medium for 2 days and experienced different NaBu treatment conditions and stained with Pax7, Ki67 and MHC antibodies. Cells in top row were not treated with NaBu. Cells in the middle row were treated with NaBu for 1 day before the induction of differentiation (Day 4 of culture). Cells in the bottom row were treated with NaBu continuously for 3 days from the day before the induction of differentiation (Day 4-6 of culture). Scale bars, 100 μm. Measurement results for the ratios of $Pax7^{+}Ki67^{+}$ and $Pax7^{+}Ki67^{-}$ cells, as well as the fusion indices are shown in the right two panels. * P < 0.05; ns, not significant.

Figure 6

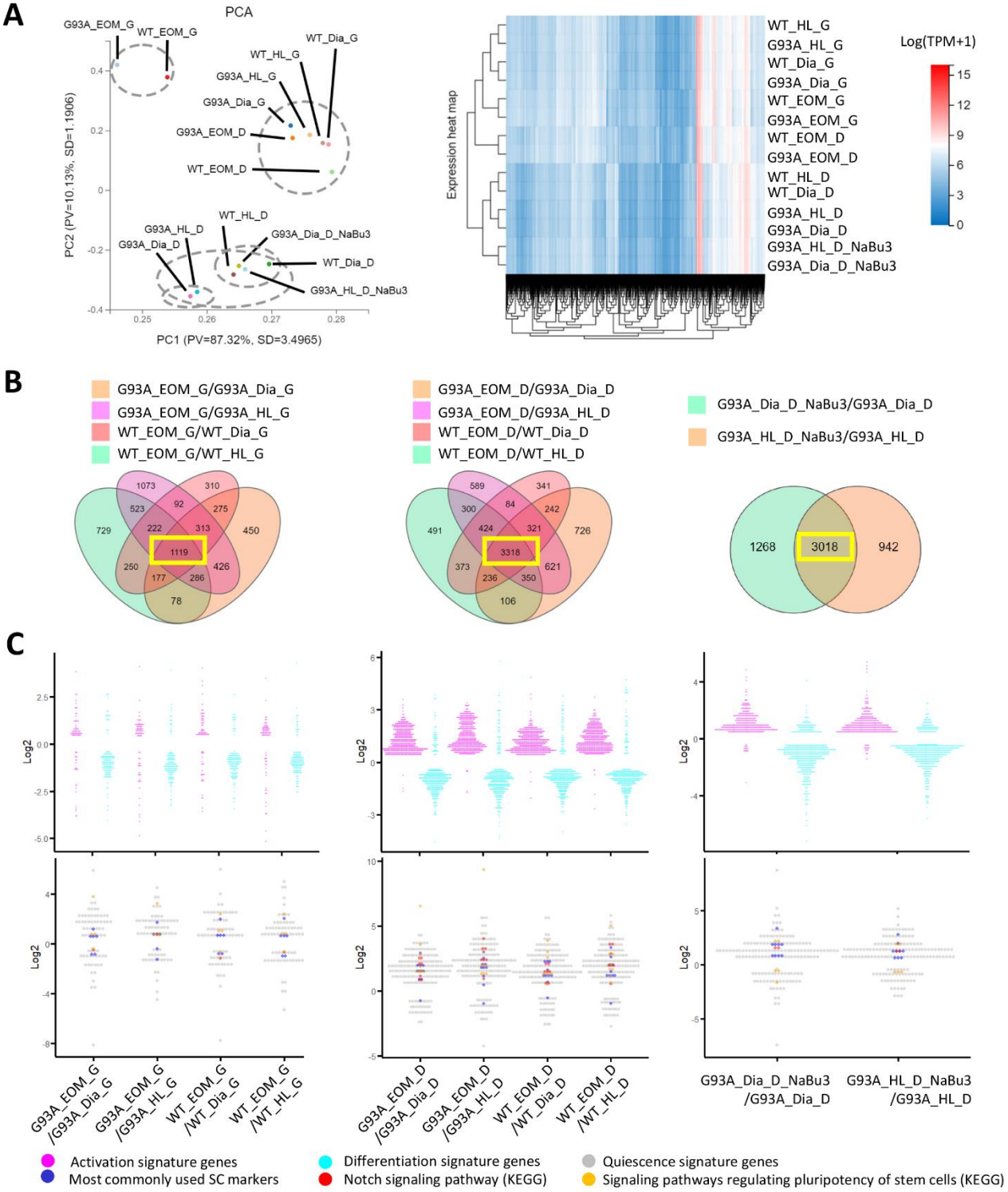
A
PCA
G93A_EOM_G
WT_EOM_G
WT_Dia_G
WT_HL_G
G93A_HL_G
G93A_Dia_G
G93A_EOM_D
WT_EOM_D
WT_HL_D
G93A_HL_D
G93A_Dia_D
G93A_Dia_D_NaBu3
WT_Dia_D
G93A_HL_D_NaBu3
PC2 (PV=10.13%, SD=1.1906)
PC1 (PV=87.32%, SD=3.4965)
Expression heat map
Log(TPM+1)
B
G93A_EOM_G/G93A_Dia_G
G93A_EOM_G/G93A_HL_G
WT_EOM_G/WT_Dia_G
WT_EOM_G/WT_HL_G
G93A_EOM_D/G93A_Dia_D
G93A_EOM_D/G93A_HL_D
WT_EOM_D/WT_Dia_D
WT_EOM_D/WT_HL_D
G93A_Dia_D_NaBu3/G93A_Dia_D
G93A_HL_D_NaBu3/G93A_HL_D
1268
3018
942
C
Log2
G93A_EOM_G /G93A_Dia_G
G93A_EOM_G /G93A_HL_G
WT_EOM_G /WT_Dia_G
WT_EOM_G /WT_HL_G
G93A_EOM_D /G93A_Dia_D
G93A_EOM_D /G93A_HL_D
WT_EOM_D /WT_Dia_D
WT_EOM_D /WT_HL_D
G93A_Dia_D_NaBu3 /G93A_Dia_D
G93A_HL_D_NaBu3 /G93A_HL_D
Activation signature genes
Most commonly used SC markers
Differentiation signature genes
Notch signaling pathway (KEGG)
Quiescence signature genes
Signaling pathways regulating pluripotency of stem cells (KEGG)

Figure 6. Comparing the transcriptomic profile and homeostasis preferences of SCs from different muscle origins cultured in growth and differentiation medium. (**A**) PCA analysis and hierarchical clustering results of different RNA-Seq samples. Samples with suffix “G” were SCs cultured in growth medium for 4 days. Suffix “D” denote SCs cultured in growth medium for 4 days and differentiation medium for 2 days. Suffix “NaBu3” denote SCs treated with 0.5 mM NaBu continuously for 3 days (Day 4-6 of culture). Dashed-line circles in PCA plot highlight samples close to each other in distance. (**B**) We identify genes differentially expressed in EOM SCs compared to their diaphragm and HL counterparts cultured in growth medium (leftmost panel) and differentiation medium (middle panel) by screening for genes shared by the four DEG lists (gold, magenta, pink and green in color) shown in the Venn diagrams. All DEG lists were generated based on the standard of |log2FC|>= 0.4 and FDR<= 0.001. Yellow box highlights the shared genes. To identify NaBu treatment signature genes, we screened for genes shared by the two DEG lists (green and gold in color) shown in the rightmost Venn diagram. (**C**) Dot plots in the upper row show the Log2FC of activation signature genes (magenta) and differentiation signature genes (cyan) identified in the 1119, 3318 and 3018 genes highlighted in yellow boxes in (B). Dot plots in the lower row show the Log2 FC of quiescence signature genes identified in the yellow-box highlighted genes in (B). Additionally, genes belonging to the following subgroups of quiescent signature genes: most commonly used SC markers, Notch signaling components and pluripotency signaling components are colored in dark blue, red and gold, respectively.

Figure 7

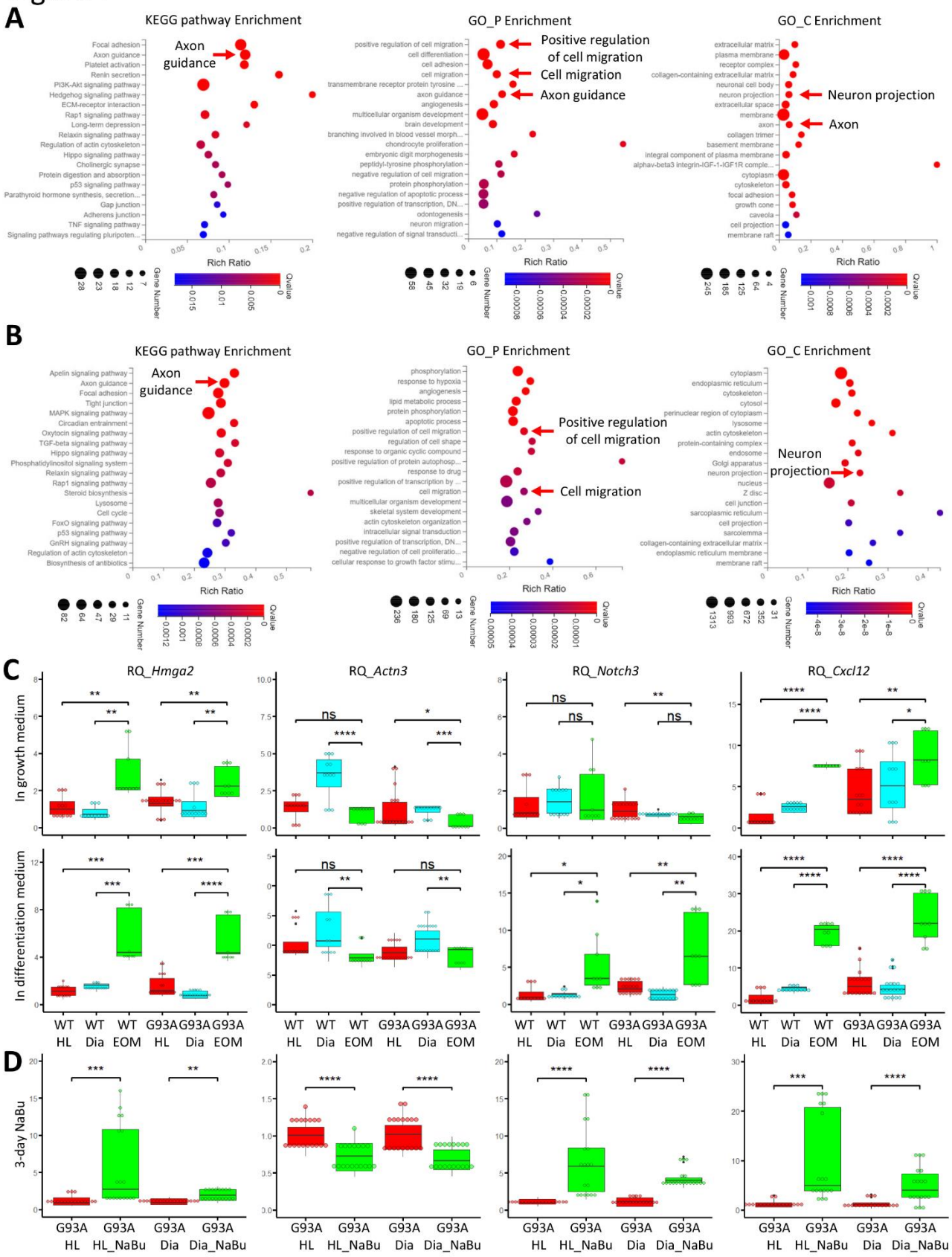
A
KEGG pathway Enrichment
Axon guidance
GO_P Enrichment
Positive regulation of cell migration
Cell migration
Axon guidance
GO_C Enrichment
Neuron projection
Axon
Rich Ratio
Gene Number
Qvalue
B
KEGG pathway Enrichment
Axon guidance
GO_P Enrichment
Positive regulation of cell migration
Cell migration
GO_C Enrichment
Neuron projection
C
RQ_Hmga2
RQ_Actn3
RQ_Notch3
RQ_Cxcl12
ln growth medium
ln differentiation medium
WT HL
WT Dia
WT EOM
G93A HL
G93A Dia
G93A EOM
D
3-day NaBu
G93A HL
G93A HL_NaBu
G93A Dia
G93A Dia_NaBu

919

Figure 7. Functional annotation analysis of EOM SC signature genes and NaBu treatment signature genes and qRT-PCR results. (**A**) Top KEGG pathway, GO_P and GO_C annotations of the 478 EOM signature genes (expressed higher in EOM SCs compared to diaphragm and HL counterparts cultured in both growth medium and differentiation medium). Arrows highlight annotations related to axon guidance and cell migration. (**B**) Top KEGG pathway, GO_P and GO_C annotations of the 3018 NaBu treatment signature genes shown in Figure 6B, rightmost panel. (**C**) qRT-PCR based relative quantification of *Hmga2* (activation signature gene), *Actn3* (differentiation signature gene), *Notch3* (quiescence signature gene) and *Cxcl12* (axon guidance molecule) expression in HL, diaphragm and EOM SCs cultured in growth and differentiation medium, respectively. * $P < 0.05$; ** $P < 0.01$; *** $P < 0.001$; **** $P < 0.0001$; ns, not significant. RNA samples were collected from 3-6 rounds of sorting and sorted cells were split into 3 replicates. (**D**) qRT-PCR based relative quantification of *Hmga2*, *Actn3*, *Notch3* and *Cxcl12* expression in G93A HL and diaphragm SCs with or without the 3-day NaBu treatment. RNA samples were collected from 6 rounds of sorting and sorted cells were split into 3 replicates.

Figure 8

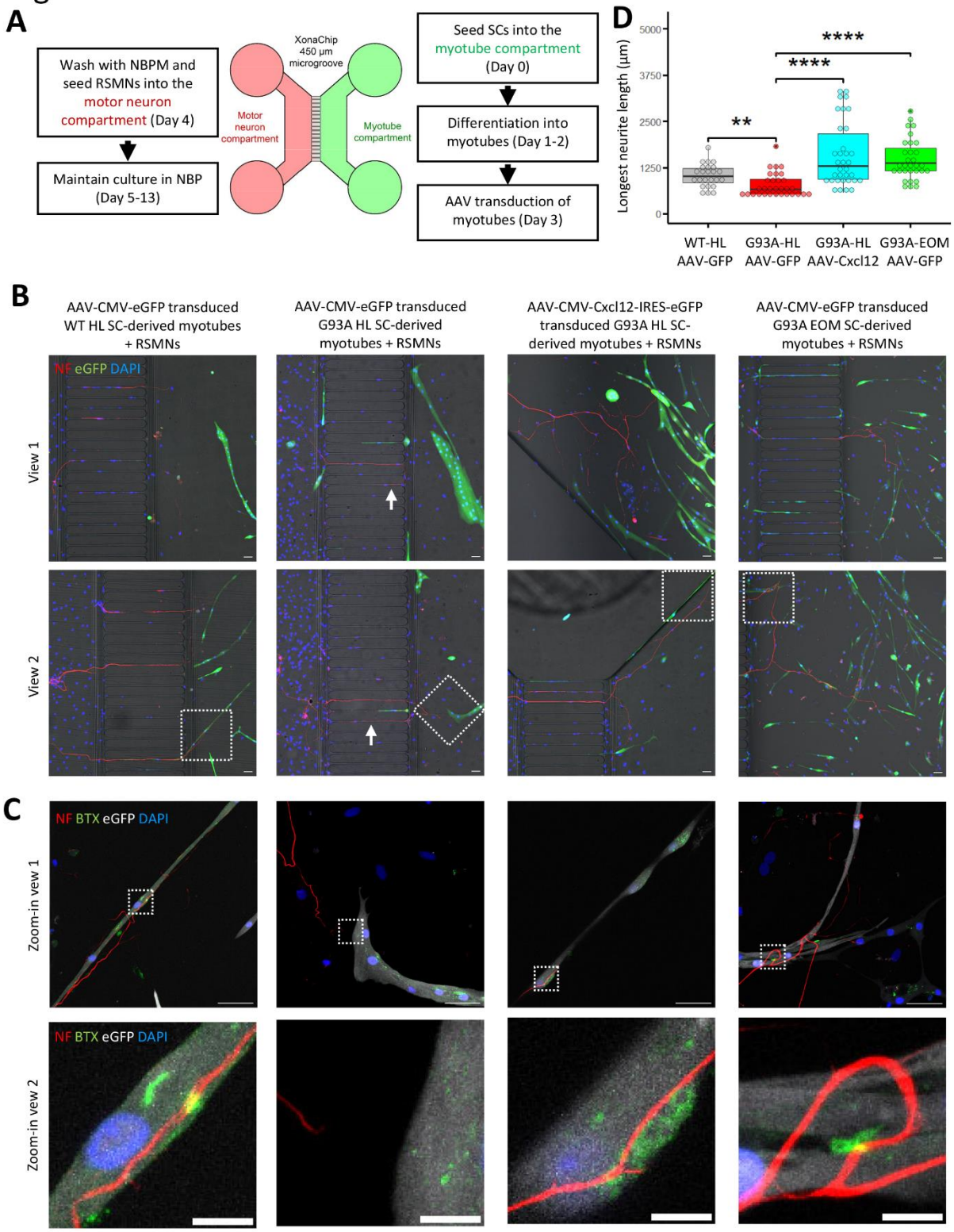

934

935

936

Figure 8. Coculture of AAV transduced SC derived myotubes with rat spinal motor neurons in compartmentalized microfluidic chambers. (A) Schematic representation of XonaChip spatial configuration and coculture experiment timeline. NBPM: Neurobasal Plus Medium; RSMNs: rat spinal motor neurons. **(B)** Representative composite images of RSMNs cocultured with: 1. WT HL SC-derived myotubes transduced with AAV-CMV-eGFP; 2. G93A HL SC-derived myotubes transduced with AAV-CMV-eGFP; 3. G93A HL SC-derived myotubes transduced with AAV-CMV-Cxcl12-IRES-eGFP; 4. G93A EOM SC-derived myotubes transduced with AAV-CMV-eGFP. Arrows highlight RSMN neurites crossed the microgrooves but stayed close to the edges and grew backward. Also see Figure 8-figure supplement 2A. Boxed regions are enlarged below. Scale bars: 50 μm. **(C)** Zoom-in views of RSMN neurites innervated or missed the AChR clusters (BTX positive patches). Boxed regions are further enlarged below. Scale bars: 50 μm, 10 μm. **(D)** Measured lengths of the longest neurites derived from RSMN cells (presumably axons) crossing the 450 μm microgrooves. n = 24, 31, 34,31 cells for the 4 groups, respectively (from 3 rounds of coculture experiments).

Figure 9

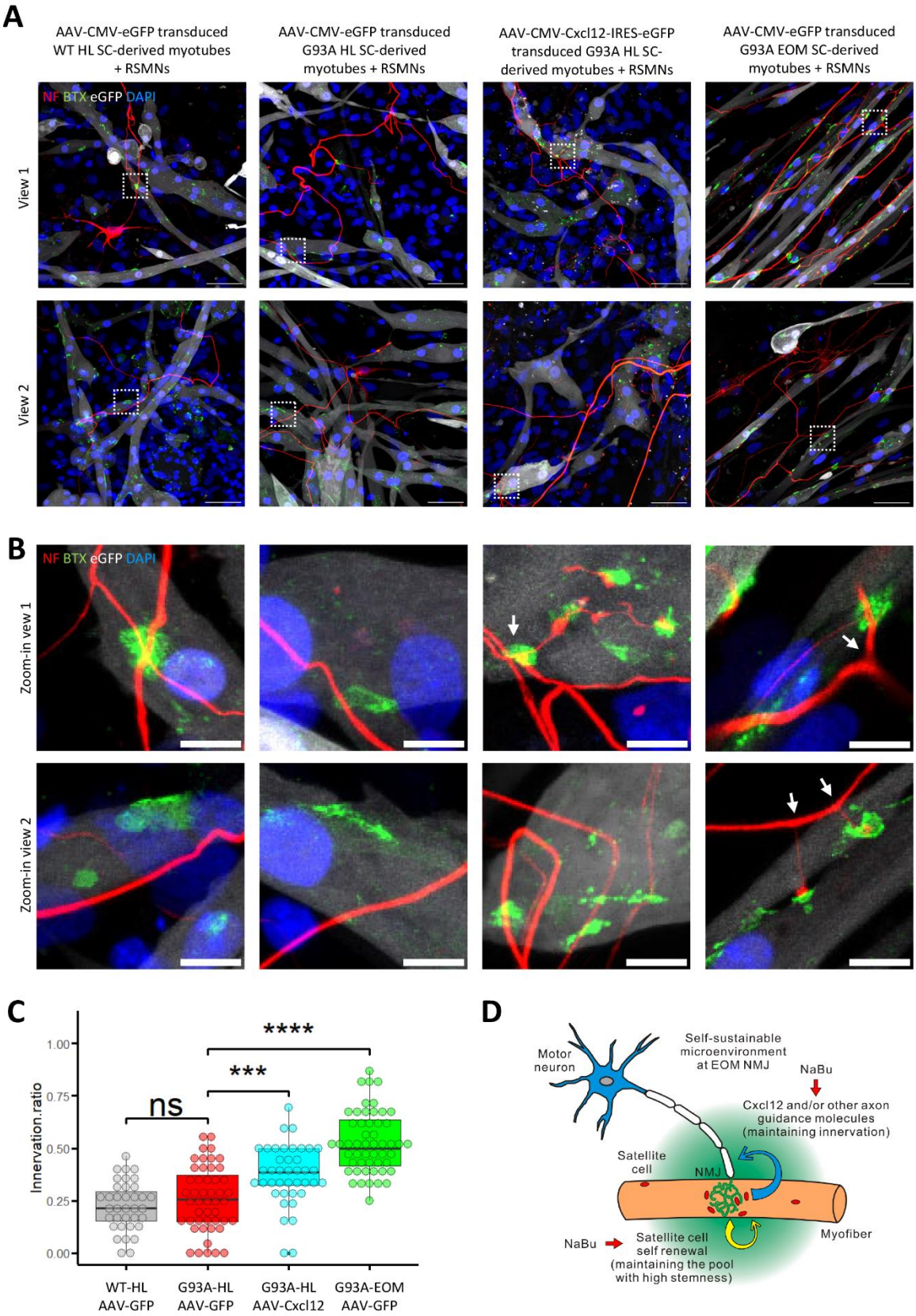
A
AAV-CMV-eGFP transduced WT HL SC-derived myotubes + RSMNs
AAV-CMV-eGFP transduced G93A HL SC-derived myotubes + RSMNs
AAV-CMV-Cxcl12-IRES-eGFP transduced G93A HL SC-derived myotubes + RSMNs
AAV-CMV-eGFP transduced G93A EOM SC-derived myotubes + RSMNs
NF BTX eGFP DAPI
View 1
View 2
B
Zoom-in vew 1
Zoom-in view 2
C
Innervation.ratio
1.00
0.75
0.50
0.25
0.00
ns
***
****
WT-HL AAV-GFP
G93A-HL AAV-GFP
G93A-HL AAV-Cxcl12
G93A-EOM AAV-GFP
D
Motor neuron
Self-sustainable microenvironment at EOM NMJ
NaBu
Cxcl12 and/or other axon guidance molecules (maintaining innervation)
Satellite cell
NMJ
Myofiber
NaBu
Satellite cell self renewal (maintaining the pool with high stemness)

950

Figure 9. Coculture of AAV transduced SC derived myotubes with rat spinal motor neurons within the same compartment. (A) Representative composite images of RSMNs cocultured with: 1. WT HL SC-derived myotubes transduced with AAV-CMV-eGFP; 2. G93A HL SC-derived myotubes transduced with AAV-CMV-eGFP; 3. G93A HL SC-derived myotubes transduced with AAV-CMV-Cxcl12-IRES-eGFP; 4. G93A EOM SC-derived myotubes transduced with AAV-CMV-eGFP. The timeline was the same as that in Figure 8 but RSMNs were seeded on top of myotubes. Boxed regions are enlarged in (B). Scale bars: 50 μm. **(B)** Zoom-in views of innervated and non-innervated AChR clusters on myotubes having contact with RSMN neurites. Arrows highlight branching phenomena observed in RSMN neurites innervating AChR clusters. Scale bars: 10 μm. **(C)** Quantification of innervation ratios of AChR clusters (area > 10 μm^2) in myotubes in contact with RSMN neurites. n = 37, 48, 40, 52 z-stack images for the 4 groups, respectively (from 3 rounds of coculture experiments). Also see methods for detailed description. *** $P < 0.001$; **** $P < 0.0001$; ns, not significant. **(D)** Graphic summary of the potential mechanisms contributing to EOM NMJ integrity maintenance during ALS progression mimicked by NaBu treatment.

Legends for supplementary figures and tables

Figure 1-figure supplement 1. Representative images of the three types of NMJs and qRT-PCR results of *Scn5a* expression in whole muscles. (**A**) Representative images of well-innervated, partially innervated and poorly innervated NMJs in WT diaphragm muscles. BTX: Alexa Fluor 488 conjugated α-Bungarotoxin; SYP: synaptophysin; NF: neurofilament medium chain. (**B**) qRT-PCR based relative quantification of *Scn5a* expression using RNAs extracted from whole muscles of EDL, soleus, diaphragm and EOM. * $P < 0.05$; ** $P < 0.01$; ns, not significant.

Figure 1-table supplement 1. Quantification results of the three types of NMJs in muscles of different origins and treatment conditions.

Figure 1-table supplement 2. qRT-PCR results for *Scn5a* relative expression in whole muscles of different origins and treatment conditions. The calculation of ddCt used the averaged dCt value of *Scn5a* of EDL muscles derived from WT mice as the normalization control.

Figure 2-table supplement 1. Quantification results of averaged peri-NMJ SC numbers in muscles of different origins and treatment conditions.

Figure 3-figure supplement 1. Representative FACS profiles of single antibody staining controls. (**A**) FACS profile of cells isolated from WT HL muscles and stained only with PE conjugated anti-mouse Vcam1 antibody at 600 ng/10^6 cells. FSC-H/SSC-H, FSC-A/SSC-A, SSC-H/SSC-W, FSC-H/FSC-W, Time/FSC-H, Vcam1/CD31_CD45_Sca-1 plots, CD31_CD45_Sca-1 count histogram and Vcam1 count histogram are shown on the left. Population hierarchies were shown on the right. (**B**) FACS profile of cells stained only with APC conjugated anti-mouse CD31 antibody at 400 ng/10^6 cells. (**C**) FACS profile of cells stained only with APC conjugated anti-mouse CD45 antibody at 400 ng/10^6 cells. (**D**) FACS profile of cells stained only with APC conjugated anti-mouse Sca-1 antibody at 200 ng/10^6 cells.

Figure 3-figure supplement 2. Viability assessment of cells for sorting using methyl green. (**A**) FACS profile of unstained cells isolated from WT HL muscles. FSC-H/SSC-H, FSC-A/SSC-A, SSC-H/SSC-W, FSC-H/FSC-W, Vcam1/Methyl green, Time/FSC-H plots, Methyl green count histogram and Vcam1 count histogram are shown on the left. Population hierarchies were shown on the right. (**B**) FACS profile of methyl green stained cells with 50% dead cells (through methanol dehydration) spiked in. (**C**) FACS profile of methyl green stained cells without any spiked-in dead cells. (**D**) FACS profile of methyl green and Vcam1 double-stained cells (no dead cells spiked in).

Figure 3-table supplement 1. Percentage of P5-4 events recorded in different rounds of sorting.

Figure 4-figure supplement 1. Comparing proliferation and differentiation properties of cultured SCs from WT and G93A muscles. (**A**) Comparing the ratios of $Pax7^+Ki67^+$, $Pax7^+Ki67^-$ and $Pax7^-Ki67^-$ cells in the SCs cultured in growth medium, respectively. **** $P < 0.0001$; *** $P < 0.001$; ns, not significant. (**B**) Comparing the ratios of $Pax7^+Ki67^+$, $Pax7^+Ki67^-$ cells and fusion indices of the SCs cultured in differentiation medium, respectively. **** $P < 0.0001$; *** $P < 0.001$; * $P < 0.05$; ns, not significant.

Figure 6-figure supplement 1. Compiling the activation signature gene and differentiation signature gene lists. (**A**) Hierarchical clustering results of WT and G93A SCs cultured in growth and differentiation medium. In both cases samples cultured in the same medium condition are clustered together. (**B**) Bar chart on the left shows differentially expressed genes between SCs cultured in growth and differentiation medium, with SCs derived from WT and G93A mice analyzed separately. The Venn diagram highlights 2536 of these genes shared between WT and G93A SCs. 1187 of them expressed higher in SCs in growth medium are considered activation signature genes. The rest 1349 genes expressed higher in SCs in differentiation medium are considered differentiation signature genes.

Functional annotation analysis below highlights top KEGG pathways, gene ontology_biological processes and gene ontology_cellular components enriched in these two lists of genes, respectively.

Figure 6-table supplement 1. Three subgroups of quiescent signature genes identified in the DEG lists comparing EOM SCs to diaphragm and HL counterparts cultured in differentiation medium. Log2FC and FDR are shown and genes are ranked according to relative abundance (TPM, from highest to lowest) in WT EOM SCs.

Figure 6-table supplement 2. Three subgroups of quiescent signature genes identified in the DEG lists comparing EOM SCs to diaphragm and HL counterparts cultured in growth medium. Log2FC and FDR are shown and genes are ranked according to relative abundance (TPM, from highest to lowest) in WT EOM SCs.

Figure 6-table supplement 3. Three subgroups of quiescent signature genes identified in the DEG lists comparing G93A diaphragm and HL SCs with and without 3-day NaBu treatment. Log2FC and FDR are shown and genes are ranked according to relative abundance (TPM, from highest to lowest) in G93A HL SCs.

Figure 7-figure supplement 1. Top functional annotations of EOM SC signature genes cultured in growth medium and differentiation medium. (A) Top KEGG pathway, GO_P and GO_C annotations of the 621 DEGs more abundant in EOM SCs compared to diaphragm and HL counterparts cultured in growth medium. **(B)** Top KEGG pathway, GO_P and GO_C annotations of the 2424 DEGS more abundant in EOM SCs compared to diaphragm and HL counterparts cultured in differentiation medium.

Figure 7-table supplement 1. Axon guidance related genes (KEGG) identified in EOM SC signature genes cultured in growth medium. Log2FC and FDR are shown and genes are ranked according to relative abundance (TPM, from highest to lowest) in WT EOM SCs.

Figure 7-table supplement 2. Axon guidance related genes (KEGG) identified in EOM SC signature genes cultured in differentiation medium. Log2FC and FDR are shown and genes are ranked according to relative abundance (TPM, from highest to lowest) in WT EOM SCs.

Figure 7-table supplement 3. Axon guidance related genes (KEGG) identified in NaBu treatment signature genes. Log2FC and FDR are shown and genes are ranked according to relative abundance (TPM, from highest to lowest) in G93A HL SCs with 3-day NaBu treatment.

Figure 7-table supplement 4. qRT-PCR results for *Hmga2*, *Actn3*, *Notch3* and *Cxcl12* in SCs of different muscle origins cultured in growth medium. The averaged dCt values of the genes of interest of WT HL SCs were used as the normalization controls during the calculation of ddCt.

Figure 7-table supplement 5. qRT-PCR results for *Hmga2*, *Actn3*, *Notch3* and *Cxcl12* in SCs of different muscle origins cultured in differentiation medium. The averaged dCt values of the genes of interest of WT HL SCs were used as the normalization controls during the calculation of ddCt.

Figure 7-table supplement 6. qRT-PCR results for *Hmga2*, *Actn3*, *Notch3* and *Cxcl12* in G93A diaphragm and HL SCs with or without 3-day NaBu treatment. The averaged dCt values of the genes of interest of G93A HL SCs were used as the normalization controls during the calculation of ddCt.

Figure 8-figure supplement 1. Representative views of AAV transduced G93A HL SC derived myotubes stained with Cxcl12 and eGFP antibodies. (A) G93A HL SC derived myotubes transduced with AAV8-CMV-eGFP and stained with Cxcl12 and GFP antibodies. **(B)** G93A HL SC derived from

myotubes transduced with AAV8-CMV-Cxcl12-IRES-eGFP and stained with Cxcl12 and GFP antibodies. Boxed regions are enlarged on the right and staining patterns of individual antibody are shown below. Note the elevated Cxcl12 expression in AAV8-CMV-Cxcl12-IRES-eGFP transduced myotubes. Scale bars: 50 μm, 10 μm (enlarged images).

Figure 8-figure supplement 2. Additional representative views of neuromuscular coculture in compartmentalized microfluidic chamber. (A) Cocultures of RSMNs with G93A HL SC derived myotubes transduced with AAV8-CMV-eGFP. Boxed regions are enlarged below. Arrows highlight the RSMN axons turning back towards the neuronal compartment after crossing the 450 μm microgrooves. Scale bars: 50 μm. **(B)** Cocultures of RSMNs with G93A HL SC derived myotubes transduced with AAV8-CMV-Cxcl12-IRES-eGFP. Boxed regions are enlarged below to highlight neurites extending along myotubes located close to the microgrooves. Scale bars: 50 μm.

Figure 9-figure supplement 1. Additional representative views of neuromuscular coculture within the same compartment. (A) Cocultures of RSMNs with WT HL SC derived myotubes transduced with AAV8-CMV-eGFP. Boxed regions are enlarged on the right to highlight innervated and non-innervated AChR clusters. Scale bars: 50 μm, 10 μm (enlarged images). **(B)** Cocultures of RSMNs with G93A HL SC derived myotubes transduced with AAV8-CMV-eGFP. **(C)** Cocultures of RSMNs with G93A HL SC derived myotubes transduced with AAV8-CMV-Cxcl12-IRES-eGFP. **(D)** Cocultures of RSMNs with G93A EOM SC derived myotubes transduced with AAV8-CMV-eGFP. Boxed regions are enlarged on the right to highlight innervated AChR clusters located on the same individual G93A EOM-SC derived myotube.